POLITECNICO DI TORINO
Repository ISTITUZIONALE

OpticalField Engineering and Instrumentation in Brillouin Microscopy

Original
OpticalField Engineering and Instrumentation in Brillouin Microscopy / Tong, K., Lin, F., Yang, X., Descrovi, E., Liu, X.u., Yang, Q.. - In: ADVANCED PHOTONICS RESEARCH. - ISSN 2699-9293. - 7:11(2026), pp. 1-26. [10.1002/adpr.202500132]

Availability:
This version is available at: 11583/3017610 since: 2026-11-06T08:44:43Z

Publisher:
Wiley

Published
DOI:10.1002/adpr.202500132

Terms of use:

This article is made available under terms and conditions as specified in the corresponding bibliographic description in the repository

Publisher copyright

(Article begins on next page)

26 November 2026

Advanced Photonics Research

ADVANCED PHOTONICS RESEARCH Open Access

www.adpr-journal.com

REVIEW OPEN ACCESS

Optical-Field Engineering and Instrumentation in Brillouin Microscopy

Kangwen Tong[1,2] | Feihong Lin[1,2] | Xiaoyu Yang[1,3,4] | Emiliano Descrovi[5] | Xu Liu[1,2] | Qing Yang[1,2]

[1]State Key Laboratory of Extreme Photonics and Instrumentation, College of Optical Science and Engineering, Zhejiang University, Hangzhou, China | [2]ZJU-Hangzhou Global Scientific and Technological Innovation Center, Zhejiang University, Hangzhou, China | [3]Department of Chemical Engineering and Biotechnology, University of Cambridge, Cambridge, UK | [4]Cambridge Graphene Centre, University of Cambridge, Cambridge, UK | [5]Dipartimento di Scienza Applicata e Tecnologia, Politecnico di Torino, Torino, Italy

Correspondence: Qing Yang (qingyang@zju.edu.cn)

Received: 4 May 2025 | **Revised:** 17 August 2026 | **Accepted:** 19 October 2026

Keywords: biomedical imaging | Brillouin microscopy | inelastic scattering | label-free imaging | multimodal integration

ABSTRACT

Brillouin microscopy provides label-free optical contrast related to the high-frequency longitudinal mechanical response of materials, yet weak Brillouin signals and strong elastic background continue to limit measurement speed and precision, particularly under constrained optical exposure. Recent advances in optical instrumentation have improved the generation, discrimination, and detection of Brillouin signals. This review discusses these developments, focusing on the relationships among spectral precision, acquisition throughput, background rejection, and optical dose, as well as how different instrument architectures address specific measurement requirements and sample conditions. Emerging strategies based on optical-field control, parallel acquisition, pulsed excitation, and compact photonic integration further illustrate how optical design can improve the efficiency, measurement capability, and robustness of Brillouin microscopy.

1 | Introduction

Brillouin microscopy probes gigahertz acoustic excitations through inelastic light–matter interactions and provides spatially resolved optical contrast associated with the high-frequency longitudinal mechanical response of materials. The experimentally accessible quantities include the Brillouin frequency shift and linewidth and, in stimulated implementations, the gain or loss response. Under the corresponding optical and constitutive assumptions, the Brillouin frequency shift and linewidth can be related to the longitudinal storage and loss components of the complex longitudinal modulus, respectively. Their interpretation in terms of mechanical parameters depends on the scattering geometry as well as material quantities such as refractive index and density. Brillouin microscopy therefore provides non-contact mechanical contrast, while quantitative interpretation requires careful consideration of both optical and material contributions [1–3].

Over the past two decades, Brillouin microscopy has developed from localized spectroscopic measurements into a family of imaging approaches spanning spontaneous, stimulated, and impulsive stimulated implementations [4–7]. As these techniques matured, their physical interpretation, biomechanical relevance, and applications in biological and biomedical research have been progressively clarified and consolidated, while stimulated Brillouin approaches have continued to expand the range of accessible measurements [8–13]. Practical implementation has also become increasingly systematic through detailed protocols for the construction, calibration, acquisition, and analysis of confocal Brillouin microscopes [14]. With this foundation in place, an increasingly important question is how advances in

This is an open access article under the terms of the Creative Commons Attribution License, which permits use, distribution and reproduction in any medium, provided the original work is properly cited.

© 2026 The Author(s). *Advanced Photonics Research* published by Wiley-VCH GmbH.

optical instrumentation and optical-field control influence the performance and practical capability of Brillouin microscopy.

Advances in Brillouin microscopy increasingly involve the coordinated design of the optical source, illumination and interaction fields, collection geometry, spectral discrimination, detection, and calibration. Different architectures naturally emphasize different aspects of performance. High-extinction filtering and background-rejection strategies are advantageous when elastic background dominates [15–17], whereas spatial multiplexing is attractive for dynamic measurements requiring high acquisition throughput [18–21]. Such requirements arise in biological processes spanning markedly different timescales, including embryonic tissue deformation and morphogenesis over minutes and developmental processes extending over tens of hours [21]. Similarly, high numerical aperture improves spatial localization but changes the angular distribution contributing to the measured spectrum, making the measured spectral response dependent on both optical focusing and collection geometry. The relevance of these design choices therefore depends on the measurement requirements and sample conditions of the intended application [22–25]. Figure 1 summarizes this instrumentation-centered perspective by organizing representative optical strategies according to spectral control, spatial multiplexing, angular and polarization control, pump–probe engineering, and calibration and integration.

The following section introduces the physical principles and spectroscopic quantities relevant to the optical design and performance of Brillouin microscopy. Subsequent sections examine advances in spectral control, spatial multiplexing, angular and polarization control, pump–probe engineering, and calibration and integration, while retaining the distinctions among spontaneous, stimulated, and impulsive stimulated implementations where relevant. Representative applications are then considered in relation to the measurement requirements and sample conditions that motivate different instrument designs. Finally,

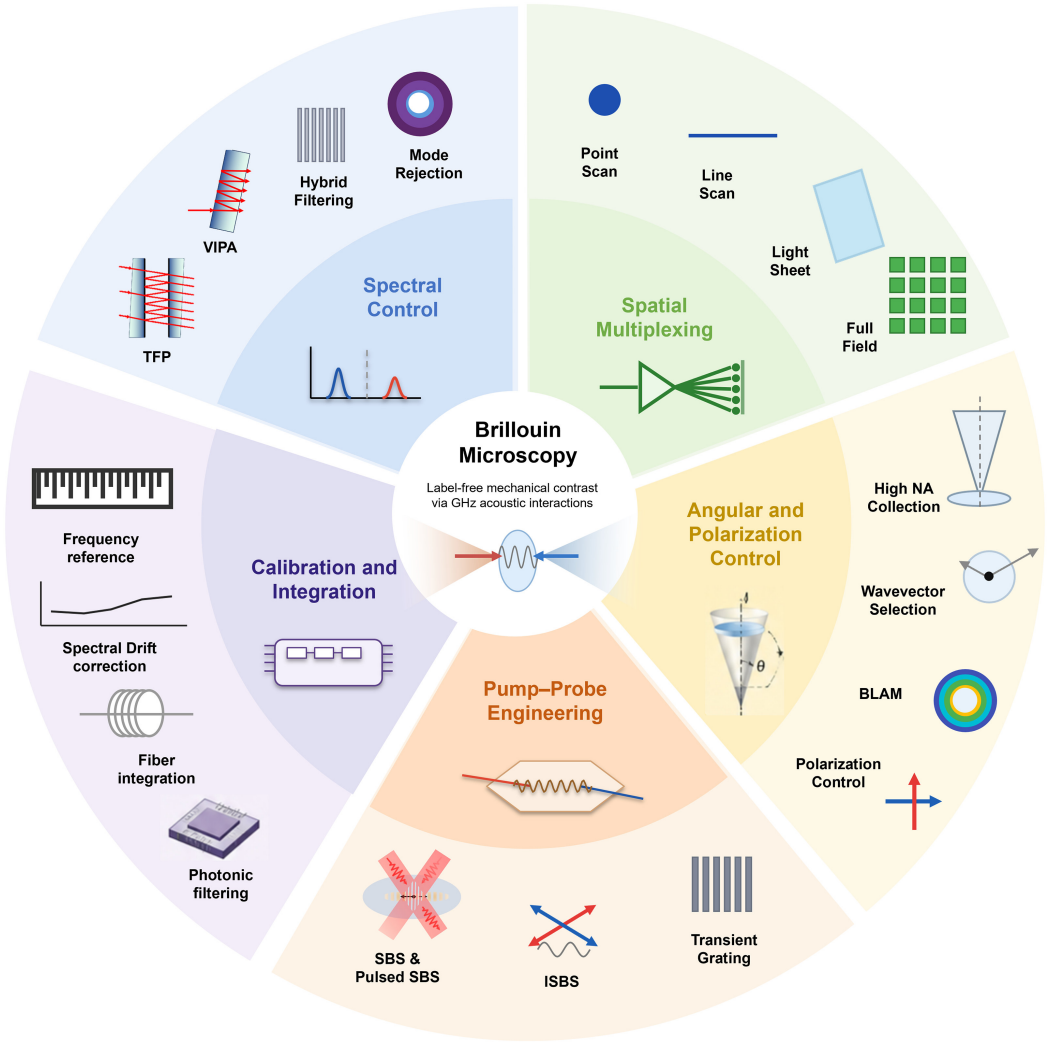


FIGURE 1 | Instrumentation-centered framework of Brillouin microscopy. Representative optical strategies are organized into five interconnected areas: spectral control, spatial multiplexing, angular and polarization control, pump–probe engineering, and calibration and integration. These strategies act at different stages of the optical measurement chain and collectively determine the spectral, spatial, temporal, and practical performance of Brillouin microscopy.

26999293, 2026, 11, Downloaded from https://advanced.onlinelibrary.wiley.com/doi/10.1002/adpr.202500132 by Emiliano Descrovi - ETH Zürich , Wiley Online Library on [06/11/2026]. See the Terms and Conditions (https://onlinelibrary.wiley.com/terms-and-conditions) on Wiley Online Library for rules of use; OA articles are governed by the applicable Creative Commons License

system-level performance, photon budget and optical exposure, and translational challenges are discussed.

2 | Instrument-Relevant Principles and Measurement Metrics

2.1 | Principles and Brillouin Observables

The experimental observation of Brillouin scattering was reported by Eugene Gross in 1930 through frequency-shifted light scattering in liquids [26]. In Brillouin microscopy, the measured response is governed by the interaction between light and acoustic excitations together with the momentum-selection condition imposed by the optical geometry. For incident and scattered optical wavevectors $\boldsymbol{k}_i$ and $\boldsymbol{k}_s$, respectively, the acoustic wavevector selected by the scattering process is:

$$\boldsymbol{q} = \boldsymbol{k}_s - \boldsymbol{k}_i \tag{1}$$

and, for an isotropic medium, its magnitude is:

$$q = \pm 4\pi n/\lambda_0 \sin\left(\frac{\theta}{2}\right) \tag{2}$$

where n is the refractive index, λ_0 is the optical wavelength in vacuum, and θ is the scattering angle. For a longitudinal acoustic mode with phase velocity V_A, the corresponding Brillouin frequency shift is

$$\nu_B = \pm 2nV_A \sin\left(\frac{\theta}{2}\right)/\lambda_0 \tag{3}$$

The measured frequency shift therefore depends on both the acoustic response of the sample and the optical scattering geometry.

In spontaneous Brillouin scattering (SpBS), thermally populated acoustic modes give rise to frequency-shifted Stokes and anti-Stokes components, as illustrated in Figure 2a. The Brillouin frequency shift reflects the frequency of the probed acoustic mode, whereas the linewidth is related to its damping and lifetime. For isotropic materials under the usual continuum description, the frequency shift can be used to determine the longitudinal storage modulus M' when the required refractive-index and density information is available, while the linewidth is required to determine the longitudinal loss modulus M'' or longitudinal viscosity [3, 27, 28]. Under the classical hydrodynamic description of simple liquids, the linewidth can be related to dissipative processes involving shear and bulk viscosities, whereas more complex materials may require descriptions beyond this simple hydrodynamic limit. Importantly, the measured linewidth can also contain contributions from finite numerical aperture, spatial heterogeneity, instrumental broadening, spectral sampling, and frequency instability. These measurement-related contributions are discussed further in Section 2.2.

Stimulated Brillouin scattering (SBS) uses controlled optical fields to coherently drive and interrogate an acoustic resonance. In a typical frequency-domain implementation, pump and probe fields are arranged so that their frequency and wavevector differences approach those of an acoustic mode in the sample. Their interference generates an electrostrictive driving force, while the induced density modulation couples the optical fields through the photoelastic effect. Near resonance, energy transfer

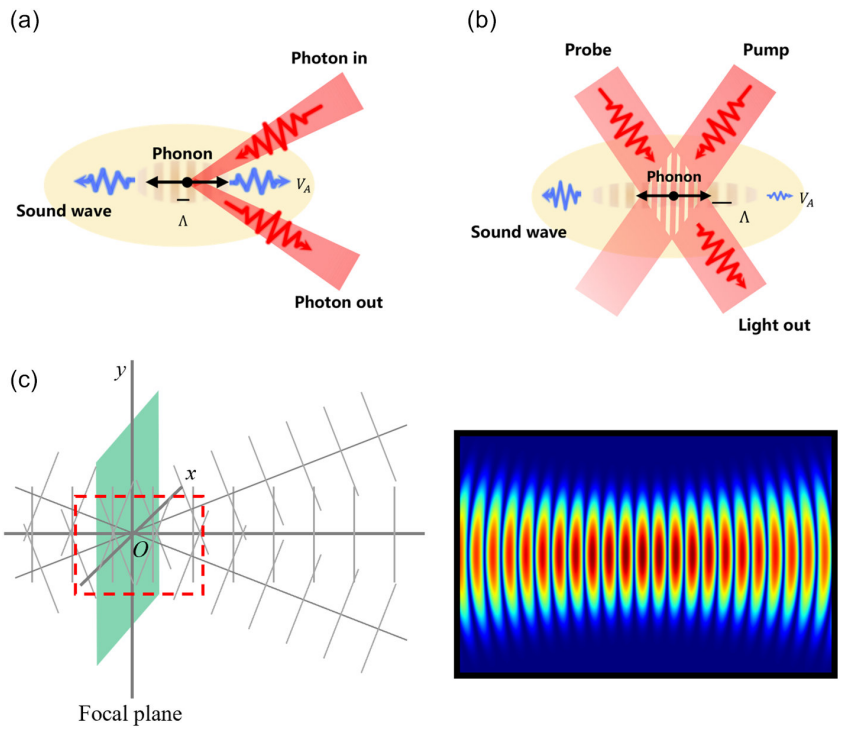


FIGURE 2 | (a) Principle of spontaneous Brillouin scattering. (b) Principle of stimulated Brillouin scattering. (c) Focused pump–probe interaction geometry and representative optical interference field near the focal region.

26999293, 2026, 11, Downloaded from https://advanced.onlinelibrary.wiley.com/doi/10.1002/adpr.202500132 by Emiliano Descrovi - ETH Zürich , Wiley Online Library on [06/11/2026]. See the Terms and Conditions (https://onlinelibrary.wiley.com/terms-and-conditions) on Wiley Online Library for rules of use; OA articles are governed by the applicable Creative Commons License

between the optical fields produces a measurable Brillouin gain or loss response, as illustrated in Figure 2b [6, 29, 30]. The first microscopic SBS imaging demonstration used a material sample consisting of water confined between glass slides, while subsequent work extended SBS microscopy to living biological specimens. In microscopy, the interaction is additionally localized by the spatial overlap of the focused pump and probe fields. Figure 2c schematically illustrates this focused interaction region, whose extent depends on the illumination and collection geometry, numerical aperture, beam overlap, and sample properties rather than on a single geometrical length scale.

Impulsive stimulated Brillouin scattering (ISBS) introduces pulsed excitation and time-domain detection. Two short pump pulses intersect in the sample to form a transient periodic intensity pattern that launches a coherent acoustic wave through electrostriction. A delayed probe field interrogates the evolving acoustic grating, and the oscillation frequency and decay of the detected signal provide access to the acoustic response [7, 31]. In contrast to frequency-domain SBS, ISBS does not require scanning the pump–probe frequency difference across the resonance. Its measurement conditions are therefore determined by parameters such as pulse duration, pump crossing angle, probe size, temporal synchronization, and spatial overlap.

The optical geometry also influences the spectrum recorded by a Brillouin microscope. Increasing numerical aperture changes the range of scattering wavevectors collected from the focal region and can consequently broaden or reshape the measured spectrum. Such finite-aperture effects have been demonstrated for spontaneous Brillouin imaging and for SBS microscopy, where changes in numerical aperture affect the measured frequency shift, linewidth, gain, and spectral lineshape [22, 25]. Spatial localization and spectral response should therefore be considered together with the illumination and collection geometry rather than be attributed to the spectrometer alone. These principles establish the physical basis for the measurement metrics discussed in Section 2.2 and for the optical architectures considered in the following sections.

2.2 | Spectroscopic Parameters and Information Processing

As introduced in Section 2.1, Brillouin microscopy extracts information from spectral quantities including the Brillouin frequency shift, linewidth, and, in stimulated implementations, the gain or loss response [3, 6, 12, 32, 33]. These observables provide information on the high-frequency longitudinal mechanical response of the sample, while their quantitative interpretation depends on the scattering geometry and on material parameters such as the refractive index and mass density. For isotropic samples with a known refractive index and mass density, the longitudinal acoustic velocity can be derived from the Brillouin frequency shift. Under the corresponding optical and constitutive assumptions, the real component of the complex longitudinal modulus can then be estimated: $V_A = \sqrt{M'/\rho_0}$. Additionally, the Brillouin linewidth Γ_B contains complementary information on acoustic damping and phonon lifetime and can be used to estimate the phonon coherence length: $l_c \sim \Lambda v_B/\Gamma_B$ (Λ is the phonon wavelength). Under appropriate hydrodynamic assumptions, it can also be related to the longitudinal viscosity η and the imaginary component of the complex longitudinal modulus M'' [3, 12, 34, 35].

$$\Gamma_B = q^2\eta/2\pi\rho_0 \tag{4}$$

$$M'' = 4\pi^2\rho_0 v_B\Gamma_B/q^2 \tag{5}$$

At the instrument level, spectral resolution, spectral precision, and spectral accuracy describe different aspects of the measurement performance. Spectral resolution characterizes the smallest frequency change that produces a detectable change in the measurement and is important for distinguishing closely spaced spectral features. Spectral precision describes the repeatability with which Brillouin parameters such as the frequency shift and linewidth can be determined from repeated measurements under specified acquisition conditions, whereas spectral accuracy reflects their agreement with calibrated or reference values [3, 36]. These quantities are related but not interchangeable, and their distinction is important when different spectrometer architectures or acquisition conditions are compared.

When the refractive index and density of the sample are unknown, additional measurements may be required for quantitative interpretation. For example, the local refractive index can be determined using co-localized Brillouin scattering measurements at two different scattering geometries [37]. However, due to the limitations of the detection parameters and precision in Brillouin microscopy itself, better experimental results can be obtained through multimodal fusion. For example, for samples that satisfy the assumption of a two–material mixture model, optical diffraction tomography (ODT) can be used to quantify the local refractive index distribution in biological samples, and the sample density distribution can be calculated based on the measured refractive index [38–41]. For samples with significant spatial refractive-index heterogeneity, Raman spectroscopy can provide complementary chemical and compositional information that assists the interpretation of Brillouin-derived mechanical contrast [35, 42–44].

As a crucial part of Brillouin microscopy, the extraction and analysis of spectral information have been continuously developing recently. To mitigate the temporal instability in spectral measurements of current Brillouin microscopy systems arising from thermal expansion shifts, an electro-optic modulator (EOM) can provide an internal frequency reference, spectrometer calibration, and active compensation of spectral drift. A recently published EOM-based Brillouin microscope demonstrated stable automated measurements for more than 2 days, replacing the unpublished reference used in the previous version [45].

The measured spectral signals require further processing to eliminate redundant information and enhance the signal-to-noise ratio (SNR). Elastic background arising from unwanted elastic scattering, stray light, reflections, and other spectral contributions can obscure the Brillouin signal. Background subtraction and normalization procedures are, therefore, commonly applied before spectral analysis. In subsequent spectral data analysis, curve-fitting techniques were frequently utilized to identify the characteristic parameters of the spectral peaks. Traditional methods, such as Lorentzian line fitting, can be sensitive to variations in the SNR. To enhance performance in low SNR environments (where SNR ≥ 1),

26999293, 2026, 11, Downloaded from https://advanced.onlinelibrary.wiley.com/doi/10.1002/adpr.202500132 by Emiliano Descrovi - ETH Zürich , Wiley Online Library on [06/11/2026]. See the Terms and Conditions (https://onlinelibrary.wiley.com/terms-and-conditions) on Wiley Online Library for rules of use; OA articles are governed by the applicable Creative Commons License

researchers have developed preprocessing techniques based on wavelet transforms and maximum entropy reconstruction, effectively extracting spectral features [46].

A new model selection approach has been introduced to address limitations in single-peak fitting methods, particularly their inability to distinguish mechanical properties in multi-material regions of samples. This approach combines the Akaike Information Criterion (AIC) with a physical statistical threshold based on the half-width of the water Brillouin peak (approximately 190 MHz). This method aids in selecting between single-peak and multi-peak Lorentzian models, improving the mechanical specificity and the precision of frequency shift quantification in Brillouin imaging [47].

In addition to traditional fitting strategies, non-fitting analysis methods such as spectral phasor analysis provide a fitting-free representation of Brillouin spectral information [48]. Spectral-moment analysis has also been used to extract and map spectral information without relying exclusively on conventional peak fitting [49, 50]. Another non-fitting technique, the matrix pencil algorithm, directly extracts parameters like frequency and attenuation coefficients from time-domain signals via matrix decomposition. For ISBS, an adaptive noise-suppression Matrix Pencil method has been demonstrated for weak and multi-component signals [51]. Furthermore, principal component analysis (PCA) combined with k-means clustering can be employed for preprocessing and analyzing high-dimensional spectral data in biological samples [50, 52, 53]. Overall, these optimized algorithmic designs can improve analysis efficiency and support the interpretation of heterogeneous Brillouin datasets.

3 | Optical Instrumentation and Field Engineering in Brillouin Microscopy

The performance of Brillouin microscopy depends not only on the underlying light–acoustic interaction but also on how the optical field is delivered to the sample and how the frequency-shifted signal is collected, separated from elastic background, and encoded for detection. Accordingly, the following sections discuss advances in spectral discrimination, spatial multiplexing, angular and polarization control, pump–probe excitation, and system calibration within spontaneous, stimulated, and impulsive stimulated Brillouin microscopy [2, 3].

3.1 | Spontaneous Brillouin Microscopy

3.1.1 | Spectral Discrimination and Elastic-Background Rejection

A central requirement in spontaneous Brillouin microscopy is the discrimination of frequency-shifted Brillouin light from elastic background. In practical measurements, a strong elastic background can arise from stray light, surface reflections, optical inhomogeneities, and incomplete rejection of the excitation field. Its magnitude therefore depends strongly on both the optical system and the sample and should not be interpreted simply as an intrinsic intensity difference between Brillouin and Rayleigh scattering [3, 16].

Multi-pass Fabry-Pérot (FP) interferometers were first used as a common means for extracting Brillouin signals. Brillouin spectroscopy based on tandem TFP has been reported for applications in applied physics, materials science, biomedicine, and environmental sensing [4]. Its core component, the FP interferometer, is an instrument that uses the principle of light interference to measure spectra. It consists of two parallel, partially reflective mirrors, forming a resonant cavity. When light enters this cavity, it reflects multiple times between the two mirrors, forming multi-beam interference, and the intensity of the transmitted light depends on the wavelength of the light and the distance between the mirrors. TFP generally uses two FP cavities in series and multiple optical passes to improve contrast. It also uses piezoelectric transducers to actively control the movement and alignment of the mirrors in real time. The contrast of traditional multi-pass FP interferometers is limited by stray light and back reflections, with extinction ratios typically reaching only ~100 dB [54]. The TFP-2HC spectrometer, as shown in Figure 3a, introduces a polarizer and a quarter-wave plate before each pass through the FP cavity to convert the incident light into circularly polarized light. Due to the reversal of polarization direction, the reflected light is blocked by the subsequent polarizer, effectively suppressing backscatter. Additionally, spatial filters isolate the two FP cavities, reducing crosstalk and further suppressing background noise, achieving an extinction ratio of ~150 dB [54].

The virtually imaged phased array (VIPA) is a specialized FP etalon that spatially disperses closely spaced optical frequencies and maps them to different positions on the detector. VIPA-based confocal Brillouin microscopy enabled parallel camera-based spectral detection and subsequently became widely used in biological imaging [5]. Since single VIPA spectrometers exhibit low extinction for strong elastic signals, cascading multiple VIPAs has increasingly become a popular solution. Using three VIPAs can achieve up to 80 dB extinction ratio and sub-GHz spectral resolution, with a free spectral range of 33 GHz [56].

However, considering that cascaded VIPA systems are bulky and difficult to align, some approaches reuse a single VIPA while maintaining the functionality of multistage dispersion. One VIPA recirculation design uses beam polarization control and path folding techniques to make the same beam pass through a single VIPA etalon multiple times, as shown in Figure 3d. In the optical path system, a polarizing beam splitter and a half-wave plate were used to modulate the polarization. During successive passes, the same VIPA etalon disperses the light along orthogonal spatial axes. This setup is equivalent to the traditional dual-etalon cross-axis design and achieves an extinction ratio of 58 dB [17].

Beyond modifying the dispersive architecture itself, additional spectral filtering can be introduced before the VIPA stages to further suppress the elastic background. In the hybrid configuration shown in Figure 3c, an FP etalon acts as a prefilter before a two-stage VIPA spectrometer. The FP stage suppresses excitation leakage and stray light, while the VIPA stages retain high-resolution parallel spectral dispersion and camera-based detection. The filter transmission window can be adjusted through the FP incidence angle, and matching the free spectral ranges of the FP and VIPA stages can further increase the extinction ratio [15]. Etalon-based filtering has also been used to improve elastic-background rejection in highly scattering samples

26999293, 2026, 11, Downloaded from https://advanced.onlinelibrary.wiley.com/doi/10.1002/adpr.202500132 by Emiliano Descrovi - ETH Zürich , Wiley Online Library on [06/11/2026]. See the Terms and Conditions (https://onlinelibrary.wiley.com/terms-and-conditions) on Wiley Online Library for rules of use; OA articles are governed by the applicable Creative Commons License

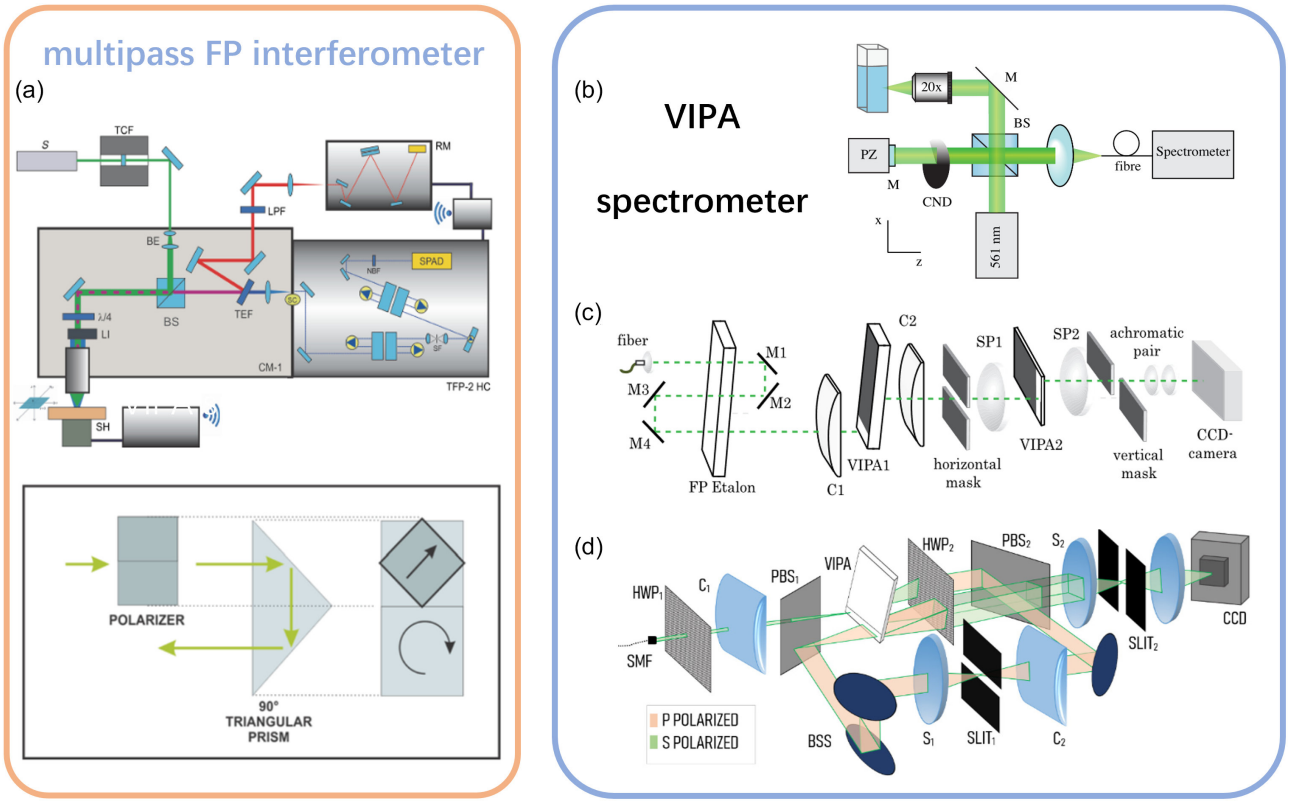


FIGURE 3 | (a) Optical system diagram of the TFP-2HC spectrometer. (b) Adjustment of the optical path difference between the two arms of the Michelson interferometer to eliminate background noise. (c) Collaborative operation of the FP etalon and VIPA. (d) A light recirculation architecture to achieve the multistage configuration. (a) Reproduced under the terms of the CC-BY Creative Commons Attribution 4.0 International license [54]. Copyright 2017, American Physical Society. (b) Reproduced with permission [55]. Copyright 2015, AIP Publishing. (c) Reproduced under the terms of the CC-BY Creative Commons Attribution 4.0 International license [15]. Copyright 2016, AIP Publishing. (d) Reprinted with permission [17]. Copyright 2019, Optica Publishing Group.

[57]. The gradient intensity filter uses a single-mode fiber as a confocal pinhole, allowing only Brillouin-scattered light from the focus to pass through, effectively suppressing out-of-focus background light. A linearly variable neutral-density filter is used to suppress VIPA sidelobe stray light, improving spectral purity. It has a high extinction ratio of 70 dB and a spectral resolution of 600 MHz [34]. Another coronagraph design transfers the technology of suppressing strong stellar light in astronomy to the field of Brillouin spectroscopy. By inserting a Lyot stop in the Fourier plane of the VIPA spectrometer, high-spatial-frequency diffraction components associated with the intense elastic field are attenuated, while the Brillouin signal is retained. This method increases the extinction ratio by approximately 20 dB with almost no additional insertion loss [58].

Another method uses dark-field illumination to suppress background noise. In this system, the angle of the incident light is different from that of the collected scattered light, so strongly reflected and elastically scattered light can be preferentially rejected before entering the spectrometer. Combined with confocal spatial filtering, this illumination geometry substantially improves discrimination of the Brillouin signal under strong-background conditions. When combined with a single-stage VIPA spectrometer, the overall extinction ratio is increased to 60 dB [16]. In addition to spatial filtering and separation methods, destructive interference can also be used to suppress elastic background. In the Michelson interferometer system shown in Figure 3b, the optical-path difference between the two arms and the amplitude of the reference light are adjusted so that elastically scattered light from the sample and the reference field undergo destructive interference before spectral detection, allowing a single-stage VIPA spectrometer to be used under strong-background conditions [55].

More recently, structured optical fields have introduced an additional degree of freedom for background discrimination. Vortex-structured-light-assisted Brillouin spectroscopy exploits differences in the spatial-mode coupling of the Brillouin signal and elastic background, providing more than 30 dB of additional background rejection under strongly scattering and highly reflective conditions [59].

The relevance of these background-rejection strategies depends on the elastic-background level, required spectral information, and acquisition conditions of the intended measurement.

3.1.2 | Spatial Multiplexing and Imaging Throughput

Imaging throughput becomes increasingly important when Brillouin spectra must be acquired over large fields of view or from dynamically changing samples. In the early development, the multi-pass FP interferometer used for Brillouin

26999293, 2026, 11, Downloaded from https://advanced.onlinelibrary.wiley.com/doi/10.1002/adpr.202500132 by Emiliano Descrovi - ETH Zürich , Wiley Online Library on [06/11/2026]. See the Terms and Conditions (https://onlinelibrary.wiley.com/terms-and-conditions) on Wiley Online Library for rules of use; OA articles are governed by the applicable Creative Commons License

spectral measurement required scanning the wavelength, which limited the speed of Brillouin imaging. Modern multi-pass TFP instruments have demonstrated acquisition times on the order of 0.5 s per spectrum [1], although sequential cavity scanning remains less suited to rapid spatial mapping than parallel spectral-detection architectures. Although non-scanning FP spectrometers shorten the data acquisition cycle by eliminating frequency scanning, introducing beam-splitting elements and light energy loss during reflection reduces throughput [2, 4, 54].

Researchers introduced the non-scanning VIPA to address this issue. As described above, it spatially disperses different optical frequencies onto different detector positions, allowing the spectrum to be acquired in parallel with a camera and substantially reducing the signal-acquisition time for a single point. At the same time, the back of the VIPA is designed with a highly reflective coating, retaining only a small anti-reflection window for light input, thereby reducing optical loss and improving throughput. While enhancing the spectral acquisition efficiency, stability during the imaging process is also crucial. A high-throughput Brillouin imaging system based on a multimode-fiber-coupled VIPA spectrometer has achieved an acquisition time of approximately 50 ms per spectrum in organoid imaging while improving stability [60]. Coker et al. conducted benchmark tests on the relationship between spectral quality and acquisition time, evaluating the performance of VIPA and TFPI systems across different acquisition conditions [2, 36]. When scanning overhead is factored in, the image acquisition process at the pixel level may necessitate an extended duration.

For large-area imaging, the sequential spatial sampling required by point-scanning systems can still result in long acquisition times. A line-scanning Brillouin microscopy system was designed to further improve the imaging speed. In 2016, based on a horizontal illumination-vertical detection structure, the line-scanning Brillouin microscope (LSBM) was first realized, which can simultaneously measure the Brillouin shifts of hundreds of points. Subsequently, a team developed a method to generate an illumination line by axially scanning the focus position with a tunable lens (Figure 4a). The setup employed two objectives arranged in an inverted 90° configuration for light delivery and collection. In the first acquisition mode, the illumination and detection directions are orthogonal, with the phonon propagation direction oriented at 45° to both. The second mode uses only a single objective, where the illumination, detection, and phonon directions are all parallel. This design enables the system to accommodate a wider range of experimental conditions and reduces the acquisition time for two-dimensional Brillouin imaging of millimeter-scale samples from several hours down to tens of seconds [18, 21].

To further expand the field of view and improve the measurement speed, a dual-line-scanning Brillouin microscope was developed (Figure 4b). This system employs two counter-propagating illumination lines incident on opposite sides of the sample. A flip mirror sequentially switches between these two lines, while Brillouin signals are collected in a 90° scattering geometry. This design enables multiplexed signal acquisition and minimizes redundant illumination outside the detected region. The system successfully captured mechanically induced changes in spheroids and enabled three-dimensional mechanical mapping of tumour spheroids [19].

Although the equivalent acquisition time of spatially multiplexed methods can approach the millisecond-per-pixel range, this quantity does not directly represent the photon-collection conditions of an individual spatial channel. Each simultaneously acquired channel must still collect sufficient Brillouin photons to achieve the required signal-to-background ratio and spectral precision. The practical imaging throughput therefore depends on photon collection, spatial multiplexing, optical exposure, and the precision required for the measurement. In individual camera-based implementations, camera exposure can additionally determine the temporal sampling interval [3, 19, 21].

From point to line, imaging speed has improved substantially, and full-field Brillouin microscopy based on imaging

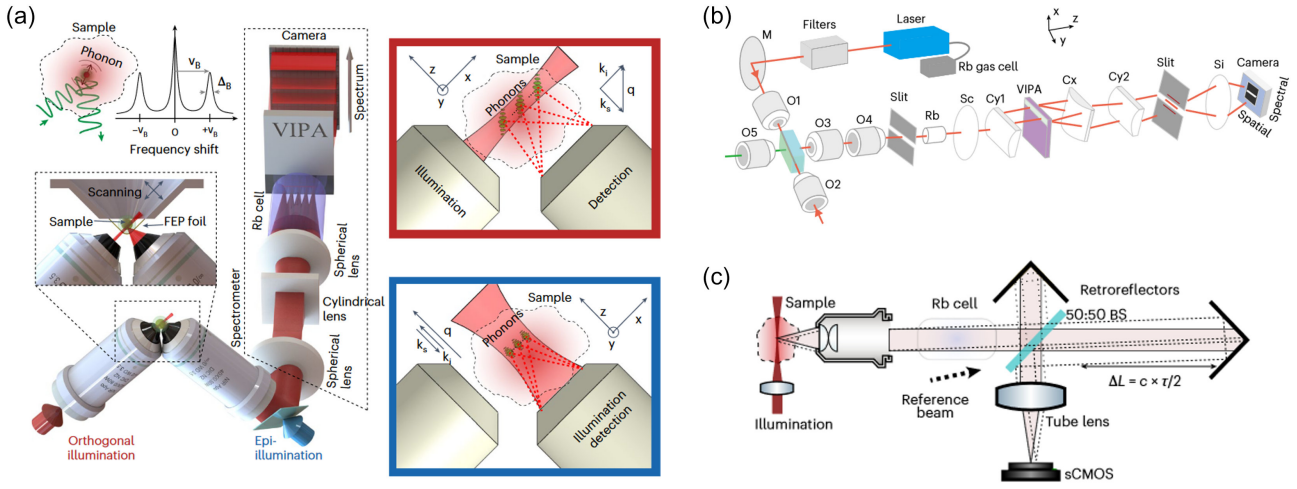


FIGURE 4 | (a) Line-scan Brillouin microscopy system. (b) Dual-line-scan Brillouin microscopy system. (c) Fourier-transform Brillouin microscopy (FTBM) system. (a) Reproduced under the terms of the CC-BY Creative Commons Attribution 4.0 International license [21]. Copyright 2023, Springer Nature. (b) Reproduced with permission [19]. Copyright 2023, Springer Nature. (c) Reproduced with permission [20]. Copyright 2025, Springer Nature.

26999293, 2026, 11, Downloaded from https://advanced.onlinelibrary.wiley.com/doi/10.1002/adpr.202500132 by Emiliano Descrovi - ETH Zürich , Wiley Online Library on [06/11/2026]. See the Terms and Conditions (https://onlinelibrary.wiley.com/terms-and-conditions) on Wiley Online Library for rules of use; OA articles are governed by the applicable Creative Commons License

Fourier-transform spectroscopy extends spatial multiplexing to a two-dimensional field. Fourier-transform Brillouin microscopy achieves an equivalent acquisition time of approximately 25 µs per pixel with a reported sample exposure time of 100 ms. Using a Fourier-transform spectrometer together with an sCMOS camera, it realizes parallel spectral acquisition over the entire two-dimensional field [20]. As shown in Figure 4c, scattered light from the sample and a reference field produce an interference signal that varies with optical-path difference. Fourier transformation of the resulting interferometric sequence enables extraction of Brillouin spectral information across the field, including both frequency-shift and linewidth information. The complete measurement should nevertheless be evaluated in terms of total optical exposure, the number of interferometric samples, and the resulting spectral precision rather than equivalent per-pixel acquisition time alone. Another full-field spectral-analysis architecture uses atomic vapour as a high-resolution spectral discriminator. This approach preserves two-dimensional spatial information at the camera while providing narrow spectral selectivity and therefore represents an alternative route toward parallel Brillouin spectral acquisition [61].

3.1.3 | *Angular, Polarization, and Wavevector Control*

Spatial resolution in Brillouin microscopy is determined primarily by the illumination and collection optics, including the numerical aperture and imaging geometry [3, 22, 25]. Imaging dimensions are not limited to 3D spatial coordinates (*xyz*). Measurements at varying angles also provide critical sample information. For instance, sample rotation can be utilized for anisotropic mechanical characterization with a fixed pump beam angle. As shown in Figure 5a, a sample (e.g., cornea) is placed in a rotatable Barron chamber, and refractive index correction converts air angles to in-tissue angles. This approach enables the detection of mechanical anisotropy in ex vivo porcine and human corneas (Figure 5b,c), achieving a lateral resolution of 0.5 µm and resolving alternating Brillouin frequency-shift bands with widths of 0.5–5 µm [23].

For fixed samples, researchers employ radial VIPAs as dispersive elements to spatially separate scattered light at different azimuthal angles onto detector arrays, acquiring multi-angle spectral information in a single exposure (Figure 5d). The resulting Brillouin Light Scattering Anisotropy Microscopy (BLAM) system achieves spatial resolutions below 2 µm and angular resolutions below 10°, revealing anisotropic mechanical responses in plant cell walls (Figure 5e) and mammalian nuclei (Figure 5f) [24].

The numerical aperture of the illumination and collection optics also determines the range of scattering wavevectors contributing to the detected spectrum. Increasing NA decreases the focal volume but simultaneously broadens the distribution of illumination and collection angles. The resulting angular averaging can contribute to broadening of the measured Brillouin lineshape [22, 25]. Polarization provides another degree of optical control. Polarization-selective components can be used to suppress unwanted reflections, while polarization-dependent stimulated Brillouin detection can exploit changes in the optical polarization state to improve signal discrimination [54, 62]. Together, angular and polarization control provide directional information that is not contained in a scalar Brillouin-frequency map.

3.2 | Stimulated Brillouin Microscopy

3.2.1 | *Continuous-Wave SBS Microscopy*

There are fundamental differences between spontaneous and stimulated Brillouin microscopy techniques. In conventional continuous-wave SBS microscopy, the Brillouin spectrum is acquired in the frequency domain by scanning the frequency difference between counter-propagating pump and probe fields across the acoustic resonance. The resulting stimulated interaction produces a gain or loss in the probe field, allowing the Brillouin frequency shift, linewidth, and gain response to be measured. Its spectral resolution primarily depends on the linewidth and frequency stability of the optical sources, while the spectral measurement range is typically determined by the available pump–probe tuning range [6, 30, 63]. Conventional SBS microscopy generally employs counter-propagating pump and probe beams in a transmission geometry. Accurate spatial overlap and frequency detuning between the two fields are therefore required, and this geometry is most straightforward for relatively thin and optically clear specimens. These requirements become increasingly restrictive for thick, opaque, or strongly scattering samples. The relevance of SBS therefore depends on the measurement requirements and sample geometry of the intended application [6, 30, 64, 65]. Because the probe and pump fields need to be strictly aligned, both two-dimensional and three-dimensional imaging commonly rely on sample or beam scanning. The spatial resolution of SBS is governed mainly by the focusing geometry, numerical aperture, and pump–probe interaction volume [25, 30, 64, 66].

3.2.2 | *Pulsed SBS and Low-Exposure Strategies*

Quasi-continuous SBS, also known as pulsed SBS microscopy, can substantially reduce the average pump power while retaining the stimulated signal and spectral precision. This technology uses an acousto-optic modulator to externally modulate the continuous-wave pump and probe light, forming 10–100 ns optical pulses, and adjusts the average power by changing the pulse duty cycle [64, 66]. The corresponding pump–probe geometry and temporal modulation are illustrated in Figure 6a. After passing through the sample, the probe light is filtered through a rubidium gas cell to remove stray light, combined with balanced detection and a lock-in amplifier, enabling high-sensitivity measurement at reduced average irradiance. In pulsed SBS, the instantaneous optical intensity during each pulse can remain sufficiently high to drive the stimulated interaction, while the time-averaged exposure is reduced through the duty cycle. Pulse duration, repetition rate, illuminated area, and average optical exposure therefore jointly define the irradiation conditions.

Quantum enhancement technology also shows potential for improving the signal-to-noise ratio at low optical power. This technology generates dual-mode intensity-difference squeezed light in a rubidium-85 atomic vapour cell through four-wave mixing.

26999293, 2026, 11, Downloaded from https://advanced.onlinelibrary.wiley.com/doi/10.1002/adpr.202500132 by Emiliano Descrovi - ETH Zürich , Wiley Online Library on [06/11/2026]. See the Terms and Conditions (https://onlinelibrary.wiley.com/terms-and-conditions) on Wiley Online Library for rules of use; OA articles are governed by the applicable Creative Commons License

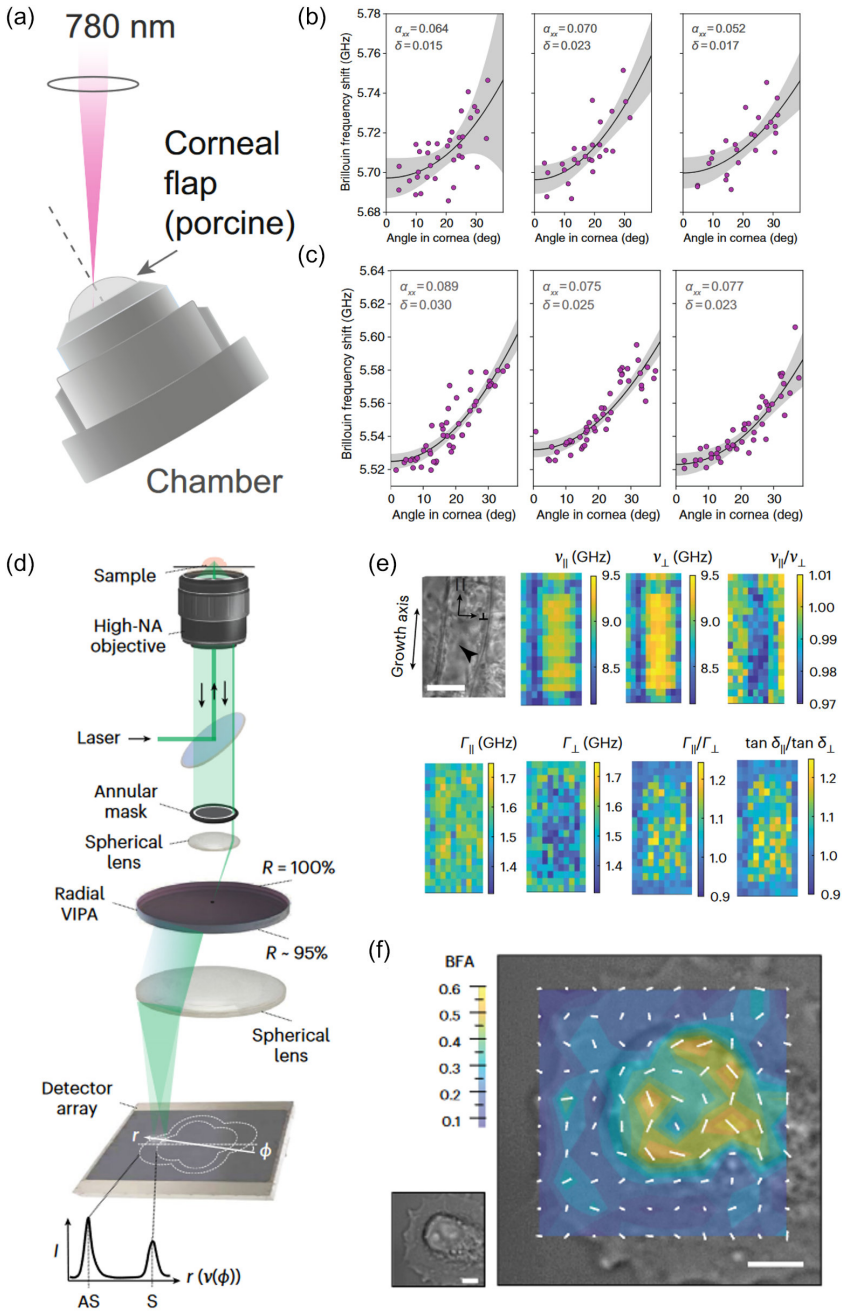


FIGURE 5 | (a) Brillouin angular dependence measurement of the cornea mounted in a Barron chamber using 0.1 NA, 780 nm beam. (b) In vivo anisotropy of Brillouin spectra in human corneal stroma. (c) Ex vivo anisotropy of Brillouin map in porcine corneal stroma. (d) Schematic diagram of Brillouin Light Scattering Anisotropy Microscopy (BLAM). BLAM-based anisotropic imaging of (e) *Arabidopsis thaliana* cell wall (Brillouin frequency shift, linewidth, and loss tangent anisotropy; scale bar 17 μm) and (f) HeLa cells (Brillouin fraction anisotropy; line length/direction corresponds to anisotropy magnitude/mean orientation; scale bar 4 μm). (a–c) Reproduced under the terms of the CC-BY Creative Commons Attribution 4.0 International license [23]. Copyright 2022, Springer Nature. (d–f) Reproduced with permission [24]. Copyright 2024, Springer Nature.

The resulting quantum correlations reduce intensity-difference noise in balanced detection [32, 68]. Under conditions where prior information about the sample is available, the spectral scanning process can be omitted, and instead, the gain at a selected frequency with mechanical contrast can be measured. This method reduces the number of sampled frequencies and can substantially shorten the acquisition time. Through filter optimization, baseline drift is suppressed, and mechanical boundaries become more clearly distinguished. Figure 6b shows the Brillouin gain measured across a glass–water interface before and after optimization of the optical filtering scheme [67].

Other methods to improve the signal-to-noise ratio, such as the polarization-pulling method, utilize the polarization dependence of SBS interactions to effectively filter signals from background light through the polarization-pulling effect. This scheme can provide an SNR 100 times higher than standard SBS receivers, but currently, only optical fibers are used as test samples [62].

26999293, 2026, 11, Downloaded from https://advanced.onlinelibrary.wiley.com/doi/10.1002/adpr.202500132 by Emiliano Descrovi - ETH Zürich , Wiley Online Library on [06/11/2026]. See the Terms and Conditions (https://onlinelibrary.wiley.com/terms-and-conditions) on Wiley Online Library for rules of use; OA articles are governed by the applicable Creative Commons License

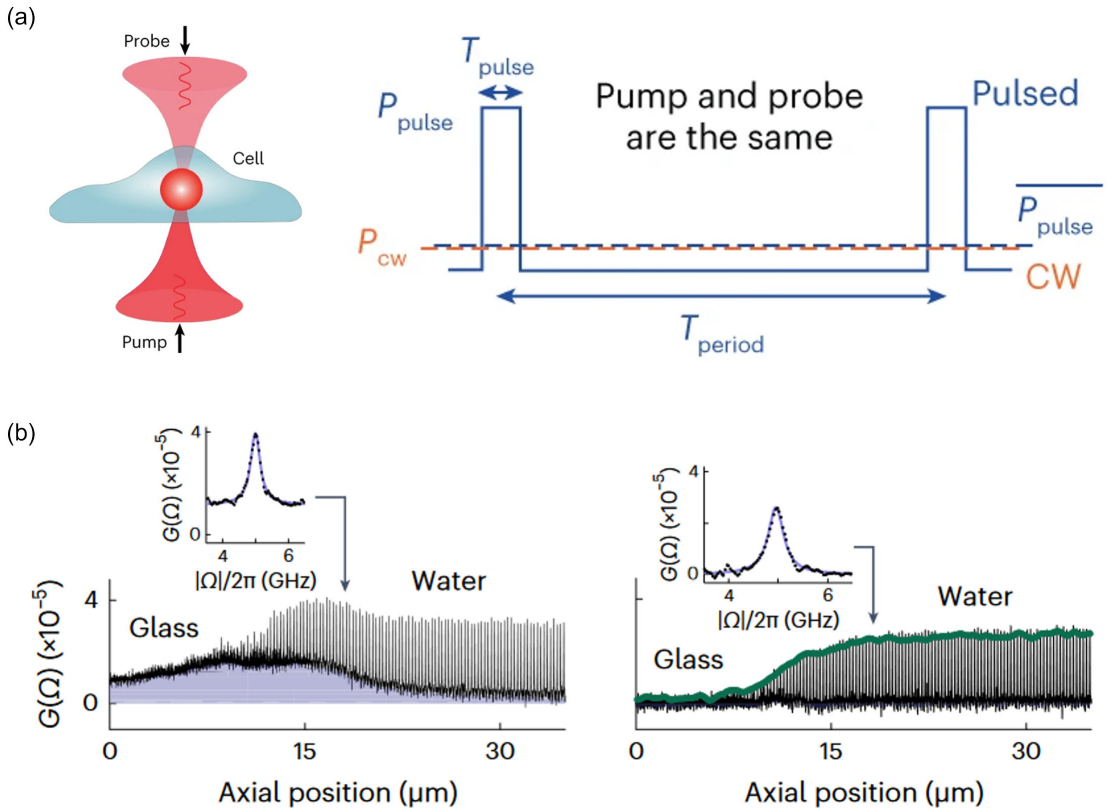


FIGURE 6 | (a) Pump–probe geometry and temporal modulation in pulsed SBS, showing the pulse duration, repetition period, peak power, and corresponding average power relative to continuous-wave excitation. (b) Brillouin gain measured across a glass–water interface before and after optimization of the optical filtering scheme; the insets show representative gain spectra. (a) Adapted under the terms of the CC-BY Creative Commons Attribution 4.0 International license [64]. Copyright 2023, Springer Nature. (b) Reproduced under the terms of the CC-BY Creative Commons Attribution 4.0 International license [67]. Copyright 2024, Springer Nature.

3.3 | Impulsive Stimulated Brillouin Microscopy

3.3.1 | Excitation and Detection

As an emerging Brillouin microscopy technology, Impulsive stimulated Brillouin microscopy has developed rapidly in recent years. Its main optical structure consists of a grating and a 4f system, as shown in Figure 7a. The pulsed pump light passes through the grating and 4f system, focusing and imaging in the focal plane (within the sample), exciting an acoustic field (transient grating). Continuous probe light enters the acoustic field range within the sample and is diffracted by the transient acoustic grating. A field derived from the same optical source and propagated through a symmetric optical path serves as a reference, producing a heterodyne beat signal with the detected probe field, as shown in Figure 7b [7, 31, 51, 69].

In terms of imaging speed, since this system excites a transient grating using an ultrashort pulsed pump laser, which manifests as broadband in the frequency domain, it can achieve resonance with multiple phonon modes without frequency sweeping. The measurement time for a single spectrum in this time-domain measurement method depends on the repetition frequency of the pulsed light and the number of averaging acquisitions. Increasing the laser repetition frequency within a specific range can enhance the measurement speed. By adjusting the repetition frequency and pulse energy, the temporal excitation conditions and average optical exposure can also be controlled, improving compatibility with biological samples [70].

Meanwhile, in heterodyne detection, multi-parameter optimization, including phase compensation, reference-light power optimization, and acquisition-time adjustment, can improve the signal-to-noise ratio. Introducing the matrix-pencil method for time-domain signal processing allows acoustic frequencies and decay parameters to be extracted with fewer averages, reducing the required integration time under appropriate signal conditions [71, 72]. Recent studies combining an exponential window function with time-domain ISBS acquisition have achieved single-shot extraction of Brillouin spectra in hydrogels, further reducing the acquisition requirements under suitable signal-to-noise conditions. Moreover, since ISBS excites phonons by projecting transient interference patterns in the sample, high-precision pump-probe focusing is not required. The stage-scanning imaging approach has the potential to be replaced by faster scanning methods (such as galvanometers), which would further increase the imaging speed [73].

3.3.2 | Optical-Field Control for Spectral and Spatial Performance

The transient acoustic grating in the ISBS is directly determined by the spatial structure of the excitation field, providing considerable flexibility for controlling its spectral and spatial performance.

26999293, 2026, 11, Downloaded from https://advanced.onlinelibrary.wiley.com/doi/10.1002/adpr.202500132 by Emiliano Descrovi - ETH Zürich , Wiley Online Library on [06/11/2026]. See the Terms and Conditions (https://onlinelibrary.wiley.com/terms-and-conditions) on Wiley Online Library for rules of use; OA articles are governed by the applicable Creative Commons License

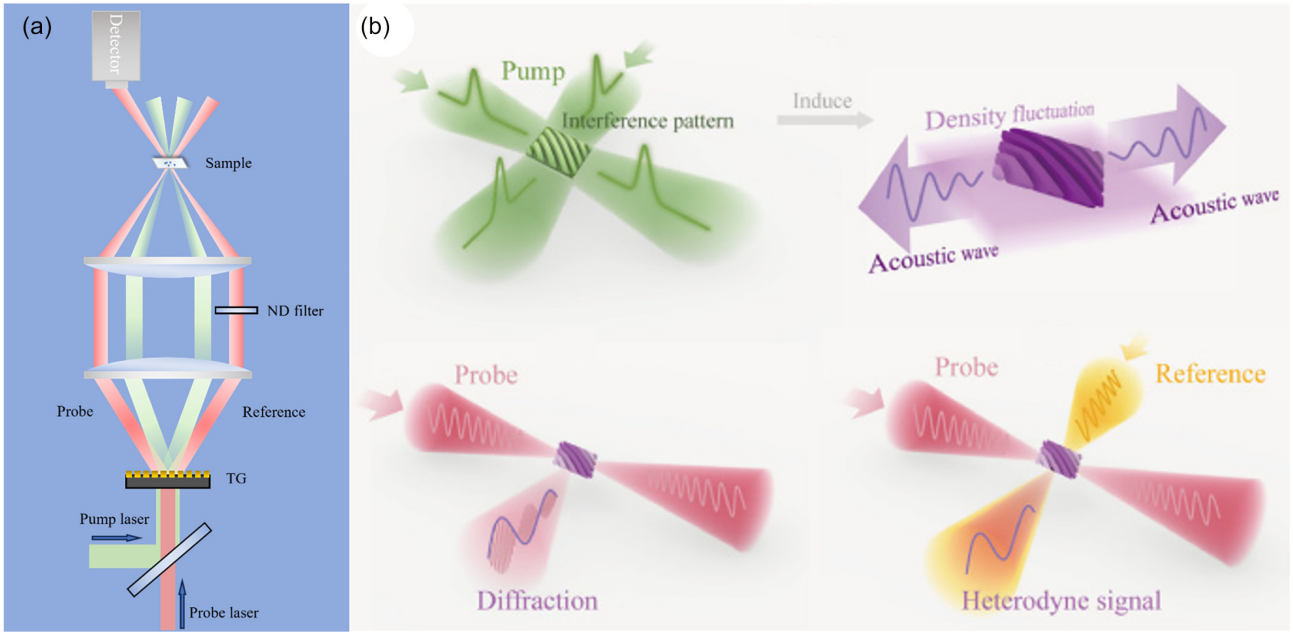


FIGURE 7 | (a) Main structure of the impulsive stimulated Brillouin microscopy system. (b) Schematic diagram of signal excitation and detection principle. (b) Adapted with permission [51]. copyright 2022, Optica Publishing Group.

By altering the initial pump-beam profile, the pump spot size in the sample and the number of illuminated grating periods can be adjusted (Figure 8a). Increasing the ratio of the linear pump-spot length d_{pump}, magnified by the telescope and cylindrical-lens system, to the initial pump-beam diameter d_0 increases the number of interference fringes in the sample, generating a longer acoustic wavepacket and reducing the temporal decay rate. This produces a narrower linewidth in the frequency domain, as shown in Figure 8b, thereby improving spectral resolution [72–75].

Recent theoretical analysis reveals that key parameters at the sample, including the incident angle, probe-beam size d_{probe}, and overlap length Δl, are related to the magnification factor of the 4f system (Figure 8c). A smaller magnification factor can reduce the probe-beam size, and replacing a conventional lens with a short-focal-length objective has reduced the lateral probe-beam dimension to approximately 7.6 μm [75]. The dependence of ISBS on optical geometry, acoustic propagation length, and interaction volume provides substantial flexibility for further optical design. Light-field modulation and beam shaping of the pump and probe fields may be used to tailor the generated grating and effective interaction volume, although these changes can also modify the interaction gain.

3.4 | Calibration, Stability, and Instrument Integration

Reliable quantitative Brillouin measurements also depend on stable calibration throughout the measurement chain. Source-frequency stability, spectrometer drift, optical alignment, and data-processing stability can influence the measured Brillouin frequency shift and linewidth. Camera-based VIPA instruments require a stable mapping between detector position and optical frequency, frequency-domain SBS requires an accurately defined pump–probe detuning axis, and ISBS requires stable temporal sampling and extraction of time-domain parameters. Electro-optic-modulator-based frequency references provide a direct route to calibration and drift correction. An EOM-integrated Brillouin microscope can use the modulator as an internal frequency reference and spectrometer-calibration standard together with closed-loop feedback, enabling stable automated measurements over extended acquisition periods [45].

Practical implementation also depends on systematic alignment, calibration, acquisition, and data-analysis procedures. Detailed protocols for confocal Brillouin microscopy and the recent community Consensus provide guidance for instrument operation and for reporting quantities including spectral resolution, spectral precision, and calibration [3, 14]. Instrument integration provides another route toward improved stability and practical operation. Multimode-fibre-coupled spectrometers can improve the stability of optical delivery, while fibre-integrated Brillouin microscopes and chip-based spectral filtering reduce the number of free-space optical elements [60, 76, 77].

4 | Applications

4.1 | Single-Modal Brillouin Microscopy

4.1.1 | Materials Science Applications: Micro-Nano Scale Mechanical Property Analysis

Brillouin scattering has a long history in materials science, where acoustic excitations provide information on elastic and dynamic properties across a wide range of condensed-matter systems [27]. The development of spatially resolved Brillouin measurements has extended these studies toward local mechanical characterization at the micrometer and submicrometer scales. Representative applications include monitoring interfacial reaction, diffusion,

26999293, 2026, 11, Downloaded from https://advanced.onlinelibrary.wiley.com/doi/10.1002/adpr.202500132 by Emiliano Descrovi - ETH Zürich , Wiley Online Library on [06/11/2026]. See the Terms and Conditions (https://onlinelibrary.wiley.com/terms-and-conditions) on Wiley Online Library for rules of use; OA articles are governed by the applicable Creative Commons License

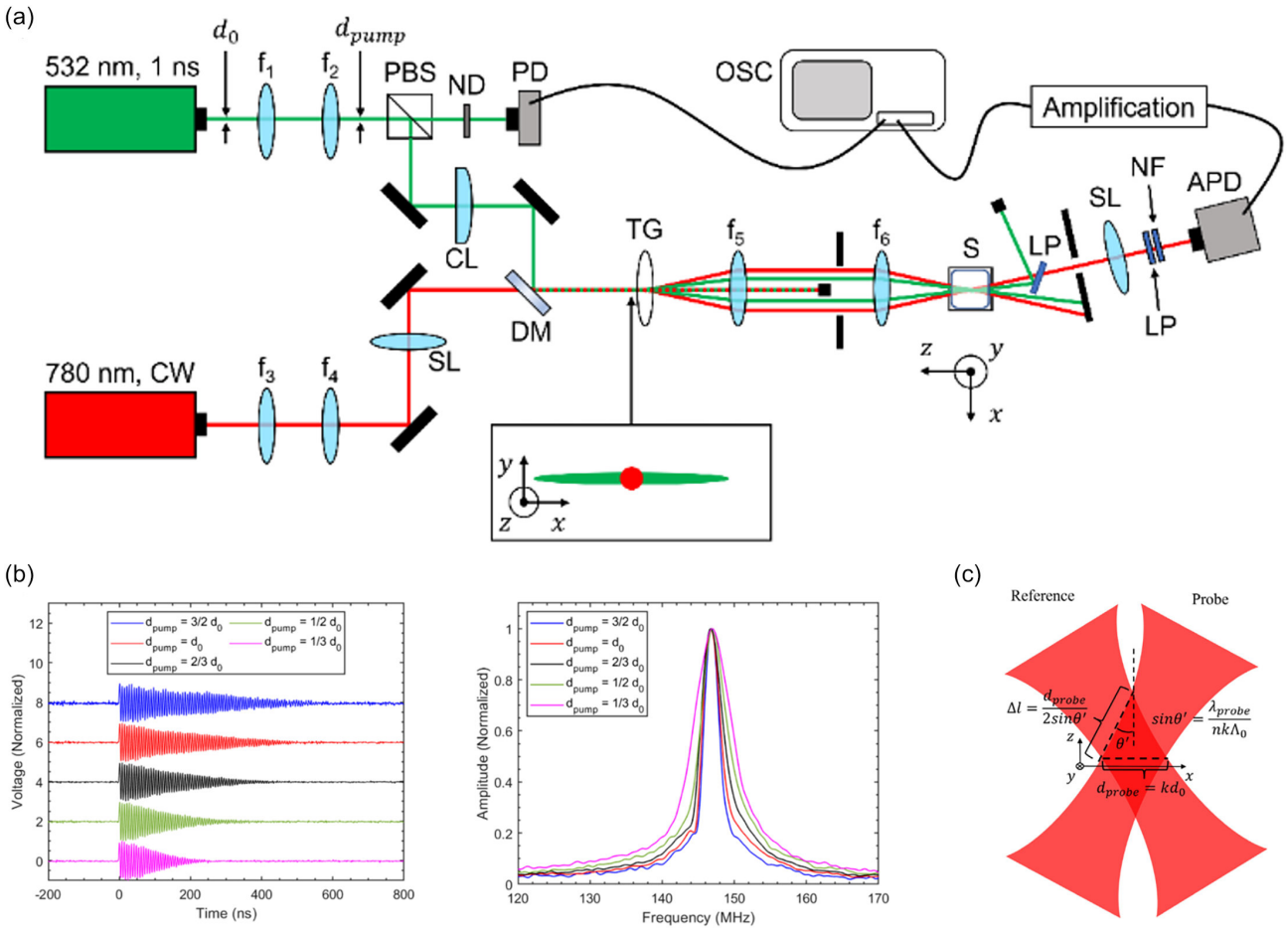


FIGURE 8 | (a) Schematic diagram of the ISBS experimental setup. The relationship between d_{pump} and d_0 is shown in the figure. (b) Effect of the ratio of d_{pump} to d_0 on the spectral linewidth of acetone. (c) Overlapping volume of the detection and reference beams at the sample. (a, b) Reprinted with permission [74]. Copyright 2023, Optica Publishing Group. (c) Reproduced under the terms of the CC-BY Creative Commons Attribution 4.0 International license [75]. Copyright 2025, Elsevier.

and polymerization in epoxy systems, characterizing elastic heterogeneity and collective dynamics in colloidal glasses, and mapping mechanical variations in hydrogels, bioprinted constructs, and engineered tissues [78–85].

Scanning micro-Brillouin light scattering further enables local spectral variations to be resolved across structurally heterogeneous materials. As illustrated in Figure 9a, spatially resolved measurements across gradient colloidal-glass structures reveal systematic changes in the vibrational modes with local particle size and mesoscopic organization [78].

Spatially resolved Brillouin light scattering has also been applied to thin films, ferroelectric materials, and magnetic microstructures, where local elastic anisotropy and spin-wave propagation can be mapped with respect to material geometry and microstructure [86–92]. Figure 9b provides a representative example in which micro-focused Brillouin light scattering resolves the spatial distribution of nanoscale spin-wave modes in a patterned magnetic structure [86]. These studies extend Brillouin measurements beyond static elastic mapping toward the characterization of propagating excitations and spatially heterogeneous responses in micro- and nanostructured materials. Non-destructive mechanical characterization has also been extended to biological materials such as plant cuticles, providing local mechanical information without physical contact with the specimen [93].

4.1.2 | Biomedical Applications: From Subcellular Mechanics to Pathological Diagnosis

In biological systems, Brillouin microscopy has been applied across scales ranging from subcellular structures to tissues and whole organisms. At the cellular scale, measurements of the cytoplasm, nucleus, nucleolus, and cytoskeleton have revealed spatial variations in mechanical response associated with cellular organization, adhesion, migration, and changes in nuclear architecture [94–98]. Brillouin microscopy has also been used to follow subcellular mechanical responses to external perturbations; for example, nanosecond pulsed electric-field stimulation produces measurable changes in the Brillouin response of the cytoplasm, nucleoplasm, and nucleolus [99].

Transparent model organisms and developing tissues provide favorable conditions for extending these measurements to multicellular systems. Brillouin imaging in *Caenorhabditis elegans*, zebrafish embryos, and developing mammalian tissues has been used to resolve mechanically distinct regions and follow

26999293, 2026, 11, Downloaded from https://advanced.onlinelibrary.wiley.com/doi/10.1002/adpr.202500132 by Emiliano Descrovi - ETH Zürich , Wiley Online Library on [06/11/2026]. See the Terms and Conditions (https://onlinelibrary.wiley.com/terms-and-conditions) on Wiley Online Library for rules of use; OA articles are governed by the applicable Creative Commons License

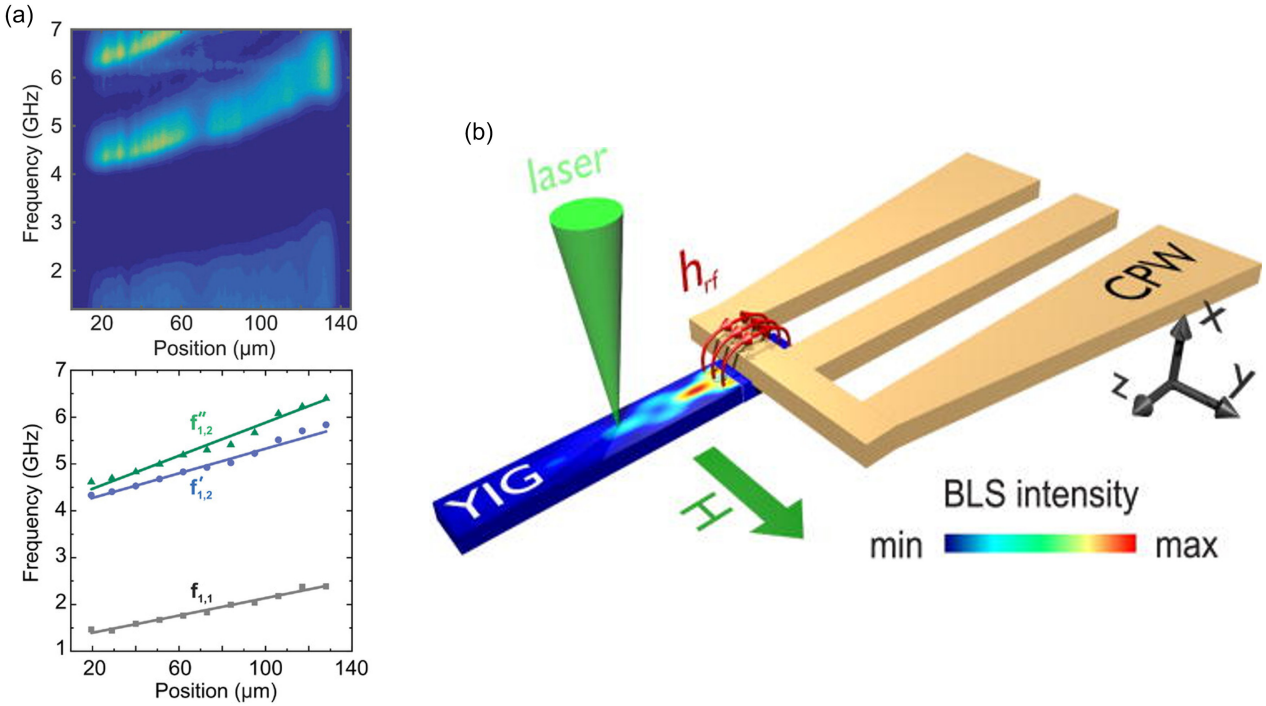


FIGURE 9 | (a) Spatial evolution of the Brillouin power spectrum and corresponding vibrational-mode frequencies measured across a gradient colloidal-glass structure. (b) Spatially resolved Brillouin light-scattering measurement of nanoscale spin-wave modes in a patterned magnetic structure. (a) Adapted under the terms of the CC-BY Creative Commons Attribution 4.0 International license [78]. Copyright 2024, Wiley-VCH GmbH. (b) Adapted under the terms of the CC-BY Creative Commons Attribution 4.0 International license [86]. Copyright 2023, AIP Publishing.

changes associated with growth and tissue differentiation [30, 64, 67, 100, 101]. Figure 10a shows a representative application of Brillouin gain microscopy in C. elegans, where measurements at selected frequency shifts provide spatially resolved mechanical contrast across the organism [67]. Beyond these model systems, Brillouin measurements have been extended to cartilage, retina, cornea, biofilms, and other tissues, demonstrating their applicability across specimens with substantially different optical and mechanical properties [102–106].

Ophthalmology is among the most established biomedical application areas of Brillouin microscopy because the transparency and layered organization of ocular tissues provide favorable optical access. Studies have investigated corneal biomechanics and anisotropy and have motivated systematic assessments of the potential of Brillouin microscopy for ophthalmic measurements [23, 105, 107–109]. More recent applications include measurements of age- and axial-length-dependent changes in the crystalline lens, biomechanical changes associated with intraocular-lens implantation, motion-tracked measurements of corneal biomechanics and subclinical keratoconus, and non-invasive mapping of retinal mechanical properties [103, 110–113].

Brillouin microscopy has also been applied to disease models characterized by spatially heterogeneous mechanical changes. In cancer research, measurements of individual cells and three-dimensional spheroids have been used to investigate mechanical phenotypes associated with migration and tumour development, while Brillouin-derived features have been explored together with machine-learning methods for mechanical classification [114–120]. Longitudinal measurements have further revealed tissue remodeling following irradiation in a radiation-cystitis model, as illustrated by the spatially heterogeneous Brillouin response of healthy and affected bladder tissue in Figure 10b [121]. In neuroscience and regenerative biology, Brillouin imaging has been used to examine mechanical changes associated with spinal-cord regeneration and brain development, including the contribution of fibroblasts and macrophages to the evolving tissue mechanical environment [122, 123].

Together, these studies demonstrate the applicability of Brillouin microscopy across biological systems spanning subcellular structures, model organisms, tissues, and disease models. The optical access, acquisition speed, spatial scale, and measurement duration required in these settings differ substantially, linking the choice of instrumentation to the biological question and sample conditions.

4.2 | Multimodal Fusion: Synergy of Brillouin Technology With Complementary Imaging Methods

Although Brillouin microscopy is highly favored for its label-free, non-contact detection of mechanical properties, it still has some unavoidable shortcomings, such as the lack of chemical specificity, insufficient morphological information, and inadequate resolution of dynamic processes (due to longer imaging times). Therefore, relying solely on single-modal studies of biomechanical properties may not provide a complete characterization of complex behaviors. The multimodal integration of Brillouin microscopy significantly expands its application potential in biomedical research. By integrating with technologies such as

26999293, 2026, 11, Downloaded from https://advanced.onlinelibrary.wiley.com/doi/10.1002/adpr.202500132 by Emiliano Descrovi - ETH Zürich , Wiley Online Library on [06/11/2026]. See the Terms and Conditions (https://onlinelibrary.wiley.com/terms-and-conditions) on Wiley Online Library for rules of use; OA articles are governed by the applicable Creative Commons License

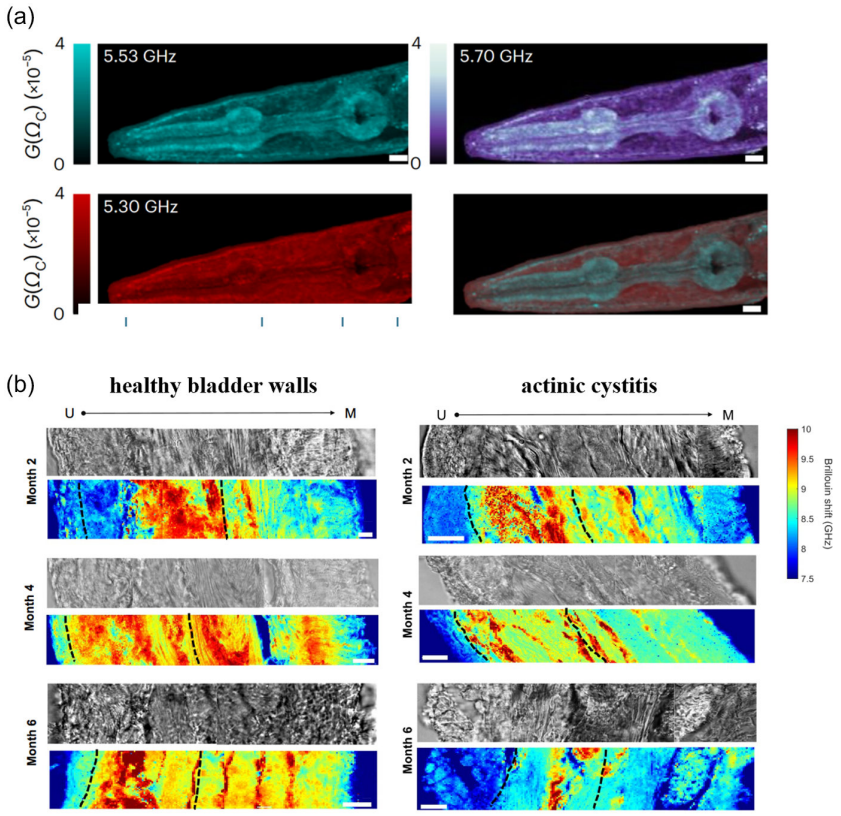


FIGURE 10 | (a) Brillouin gain microscopy of *Caenorhabditis elegans* acquired at selected frequency shifts and the corresponding integrated image. (b) Brillouin imaging of healthy and radiation-affected bladder tissue, showing spatially heterogeneous mechanical responses associated with tissue remodeling. (a) Adapted under the terms of the CC-BY Creative Commons Attribution 4.0 International license [67]. Copyright 2024, Springer Nature. (b) Adapted under the terms of the CC-BY Creative Commons Attribution 4.0 International license [67]. Copyright 2024, Springer Nature.

optical coherence tomography (OCT), fluorescence microscopy, and Raman microscopy, researchers can simultaneously acquire mechanical, chemical, and structural information, providing a more comprehensive tool for studying complex biological systems. The development and application of these combinations reflect the trend of interdisciplinary research, particularly in the fields of cellular mechanics and tissue engineering.

4.2.1 | *OCT-Brillouin Microscopy*

Optical coherence tomography (OCT) is a non-invasive, high-resolution imaging technology widely used for three-dimensional imaging of biological tissues, especially in ophthalmology for examining the retina and cornea [107]. Combined with Brillouin microscopy, this technology enables rapid acquisition of corneal structural information. A full scan with single-modal Brillouin microscopy typically takes about 20 min to complete, during which the patient's eye movements or blinking can be highly sensitive, and any slight movement may lead to data artifacts and measurement inaccuracies. In contrast, OCT imaging is fast and can monitor the cornea's axial (depth) movement in real time, providing high-precision (better than 3 microns) depth localization information to help correct errors caused by patient movement in Brillouin microscopy [112]. Additionally, OCT and Brillouin microscopy have been combined in studies of neural tube closure in mouse embryos, revealing stiffness differences in different regions of the neural tube (such as the neural tube epithelium, cochlea, and paraxial mesoderm) (Figure 11b) [125, 127, 128]. This multimodal integration technology combines the mechanosensitivity of Brillouin light with the molecular specificity of fluorescence, enabling simultaneous visualization of biomechanical and biochemical dynamics in complex environments such as the tumor microenvironment. Its importance lies in elucidating processes such as nuclear softening during cancer cell migration, which holds promise for guiding the development of anti-metastatic drugs by targeting mechanotransmission pathways. The technology's applications can also extend to clinical oncology; for example, it can enhance intraoperative decision-making, such as assessing tumor boundaries, and accelerate basic research by providing comprehensive datasets for AI-driven predictive models.

4.2.2 | *Raman–Brillouin Microscopy*

In some cases, relying solely on mechanical features cannot fully distinguish heterogeneity information in samples, and different material components may exhibit similar and indistinguishable mechanical characteristics under specific conditions or mixtures. However, each substance has its own characteristic Raman spectrum, so combining Brillouin microscopy with Raman spectroscopy can provide sufficient chemical specificity information. Recent studies using Brillouin microscopy to observe real-time changes in the mechanical properties (such as stiffness and viscosity) of subcellular structures (e.g., cytoplasm, nucleoplasm, and nucleolus) after cells are stimulated by nanosecond pulsed

26999293, 2026, 11, Downloaded from https://advanced.onlinelibrary.wiley.com/doi/10.1002/adpr.202500132 by Emiliano Descrovi - ETH Zürich , Wiley Online Library on [06/11/2026]. See the Terms and Conditions (https://onlinelibrary.wiley.com/terms-and-conditions) on Wiley Online Library for rules of use; OA articles are governed by the applicable Creative Commons License

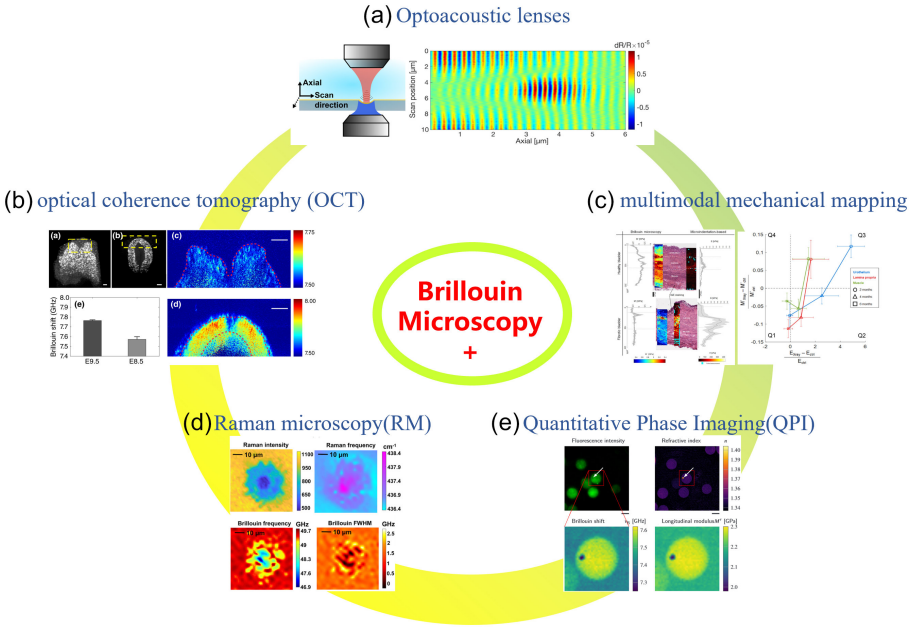


FIGURE 11 | (a) The pump light illuminating the photoacoustic lens generates a focused acoustic field, and the Brillouin scattering probe light can continuously monitor the acoustic field over time. (b) Imaging of a neural tube defect (NTD) mouse model using optical coherence tomography (OCT), Brillouin microscopy, and confocal fluorescence microscopy. (c) Validation and calibration of sample mechanical measurement results using Brillouin microscopy combined with atomic force microscopy (AFM) and optical tweezers active microrheology (OTAM). (d) Brillouin-Raman mapping experiment of ZnO samples. (e) Quantitative and spatially resolved maps of samples collected by the FOB microscope, including fluorescence intensity, refractive index, Brillouin frequency shift, and calculated longitudinal modulus. (a) Adapted under the terms of the CC-BY Creative Commons Attribution 4.0 International license [124]. Copyright 2025, Elsevier. (b) Reproduced with permission [125]. Copyright 2018, John Wiley and Sons. (c) Adapted under the terms of the CC-BY Creative Commons Attribution 4.0 International license [121]. Copyright 2024, Springer Nature. (d) Adapted under the terms of the CC-BY Creative Commons Attribution 4.0 International license [126]. Copyright 2023, DE GRUYTER. (e) Reproduced under the terms of the CC-BY Creative Commons Attribution 4.0 International license [40]. Copyright 2022, ELife Sciences Publications.

electric fields (nsPEF) confirmed, through Raman spectroscopy, that nsPEF stimulation, rather than other factors, caused the mechanical changes. The chemical stability within the focal volume was also monitored during the experiment to ensure the reliability of the results [99]. Moreover, Brillouin-Raman microspectroscopy (BRMS) has been widely used in biomedical observations, such as using Brillouin microscopy to obtain the mechanical properties of the nucleus while detecting changes in water content through Raman spectroscopy to analyze the chemical reasons for nuclear softening or for characterizing the micro-viscoelasticity of different regions of single red blood cells (RBCs) (e.g., cell edges and centers), with Raman spectroscopy assisting in verifying changes in hemoglobin content, thereby explaining changes in mechanical properties (such as decreased elastic modulus) caused by functionalization. Other biological imaging research applications include gastric cancer tissues, the morphology of the lamellar bone, and the morphological mechanics of collagen superstructures [35, 43, 129–131]. Additionally, an improved annular pupil confocal Brillouin-Raman microscope (APCBRM) technology, aimed at enhancing spectral and spatial resolution, has been validated through observations of PMMA and ZnO, demonstrating its application potential in new materials and precision machining fields (Figure 11d) [126]. This technique leverages the complementary chemical imaging information from Raman spectroscopy and the mechanical analysis information from Brillouin spectroscopy, overcoming the limitations of single-mode methods such as spectral overlap in turbid media. Its significance lies in its ability to accurately characterize material interfaces, such as nanocomposites or biocompatible implants, which is crucial for optimizing the mechanochemical synergy in tissue engineering.

4.2.3 | *Quantitative Phase-Brillouin Microscopy*

Brillouin microscopy requires the refractive index of the sample to calculate the longitudinal modulus, but it cannot directly measure the refractive index. Quantitative phase imaging (QPI) technology can measure the refractive index distribution of the sample, providing higher accuracy for calculating the internal viscoelastic properties of the sample. Recent work combining these two technologies studied the response of FUS and A1-LCD protein condensates under different temperatures, ion concentrations, and sequence variations, with QPI used for label-free measurement of protein concentration and volume fraction. By analyzing the sample's refractive index (positively correlated with protein concentration) and combining it with the known refractive index of the solvent, the protein concentration and density of the condensates can be directly calculated, providing the density parameters needed for longitudinal modulus calculation in Brillouin microscopy. Additionally, QPI can determine the geometric size of condensates through spherical fitting, helping to exclude non-specific interferences (such as surface wetting effects) [41]. Another study developed the FOB microscopy system (fluorescence imaging + optical diffraction tomography

26999293, 2026, 11, Downloaded from https://advanced.onlinelibrary.wiley.com/doi/10.1002/adpr.202500132 by Emiliano Descrovi - ETH Zürich , Wiley Online Library on [06/11/2026]. See the Terms and Conditions (https://onlinelibrary.wiley.com/terms-and-conditions) on Wiley Online Library for rules of use; OA articles are governed by the applicable Creative Commons License

ODT + Brillouin microscopy), achieving synchronous measurement of subcellular structures' refractive index, mass density (based on a two-component mixture model), and longitudinal modulus, and validated its application in living cells (Figure 11e)) [40]. Furthermore, this technology experimentally observed for the first time the dynamic softening of the nucleus during transendothelial migration (TEM) of tumor cells, supplementing knowledge of cancer cell behavior and providing new ideas for monitoring and treatment [132]. This approach carves a niche in quantitative biomechanics by decoupling refractive index from mechanical moduli, addressing a key limitation in standalone Brillouin systems for heterogeneous biological samples. Its significance is in providing accurate, multi-parameter maps (e.g., density, modulus) for studying phase-separated condensates or cellular migration, revealing novel insights into disease mechanisms like protein aggregation in neurodegeneration. The impact includes advancing precision diagnostics in oncology and neurology, potentially integrating into lab-on-chip devices for high-throughput screening, and influencing therapeutic strategies by identifying mechano-biochemical targets.

4.2.4 | Photoacoustic and Picosecond-Ultrasound Brillouin Microscopy

Acoustic information can be incorporated into Brillouin measurements through different experimental configurations. Photoacoustic (PA) microscopy has been combined with Brillouin microscopy to acquire co-registered optical and acoustic information. Shi et al. simultaneously measured Brillouin frequency shifts and time-resolved PA signals, using the PA-derived speed of sound together with the Brillouin shift to estimate the refractive index and longitudinal modulus [133]. A distinct approach uses ultrashort optical pulses to excite a photoacoustic lens and generate a focused high-frequency acoustic field, which is subsequently interrogated by time-resolved Brillouin scattering (Figure 11a). This approach achieves elastic imaging of approximately 250 nm, breaking through the limitations of the optical diffraction limit, and can monitor the propagation of sound waves in real time. Moreover, high-frequency sound waves replace the pump light in the original stimulated Brillouin microscopy pump-probe optical path, reducing light damage to the sample and providing new possibilities for high-resolution three-dimensional imaging of biological systems [124]. Picosecond ultrasonics Brillouin microscopy surpasses the optical diffraction limit through acoustic focusing, enabling imaging of nanoscale biological structures that are inaccessible to conventional optical methods. Its significance lies in its ability to monitor acoustic wave propagation in real time, thereby providing deep insights into subcellular mechanics without inducing excessive phototoxicity. This technique holds considerable clinical potential—for example, enhancing imaging of neural or vascular tissues, supporting minimally invasive diagnosis of neurological disorders, and extending into materials science for detecting defects in nanomaterials.

In addition, many multimodal fusion techniques, such as fluorescence/confocal-Brillouin microscopy, have been widely applied and are now generally integrated with earlier multimodal technologies to assist in sample detection. There are also multimodal mechanical mapping methods that use at least two different types of mechanical characterization techniques to assess the mechanical properties of samples. Experimental validations have been conducted with the fusion of atomic force microscopy (AFM) and Brillouin microscopy (BM) technology, the fusion of optical tweezers active microrheology (OTAM) and BM technology, and the synergy of optical coherence elastography (OCE) and BM (Figure 11c) [121, 134, 135]. Overall, multimodal Brillouin microscopy integrations occupy a transformative niche in hybrid imaging, bridging mechanical, chemical, and structural domains to overcome single-modality limitations in complex biological and material systems. Their significance is in enabling holistic analyses, such as correlating stiffness with molecular composition in disease models, which deepens understanding of pathophysiology and accelerates biomarker discovery. The broader impact spans clinical translation—e.g., real-time intraoperative guidance in surgery or personalized drug testing—and industrial innovation, such as quality assurance in biomaterials, potentially reducing healthcare costs and fostering AI-assisted diagnostics through richer datasets.

5 | Current Limitations and Future Development Strategies

5.1 | Balancing Imaging Quality Parameters

The performance of a Brillouin microscope cannot be represented by a single metric. Imaging speed, spatial resolution, spectral resolution, spectral precision, signal-to-noise ratio, and optical exposure are coupled through the optical architecture and measurement conditions. Table 1 summarizes representative performance parameters across selected Brillouin microscopy implementations, while Figure 12 provides a complementary visualization of the relationships among imaging speed, lateral resolution, and spectral resolution. Together, these comparisons illustrate the coupled performance trade-offs that arise under different system architectures and measurement conditions.

5.1.1 | Imaging Speed and Spatial Resolution

We can more clearly understand the relationship between the two through the statistical representation in Figure 12c and Table 1. In spontaneous Brillouin microscopy systems, the VIPA spectrometer has brought significant qualitative improvements, enhancing both performance indicators when compared to multi-pass FP spectrometers. For line-scanning implementations, spatial multiplexing substantially increases the number of sampled positions in each exposure, whereas the resulting spatial resolution remains dependent on the illumination and collection geometry, numerical aperture, and sampling strategy [19, 21].

Similarly, impulsive stimulated Brillouin microscopy eliminates frequency-domain scanning and enables rapid spectral acquisition. Its currently coarser spatial resolution is instead closely related to the spatial extent of the transient grating and the pump–probe interaction geometry. The effective interaction volume can be reduced by modifying the optical magnification and pump-beam geometry [51, 72, 75], while spatial beam shaping provides an additional degree of freedom for controlling the transient-grating distribution

26999293, 2026, 11, Downloaded from https://advanced.onlinelibrary.wiley.com/doi/10.1002/adpr.202500132 by Emiliano Descrovi - ETH Zürich , Wiley Online Library on [06/11/2026]. See the Terms and Conditions (https://onlinelibrary.wiley.com/terms-and-conditions) on Wiley Online Library for rules of use; OA articles are governed by the applicable Creative Commons License

TABLE 1 | Representative performance parameters of selected Brillouin microscopy implementations.

Technology	Representative spatial resolution	Spectral resolution, MHz	Brillouin-shift precision, MHz	Acquisition metric	Reference
TFP interferometer	1–2	100–350	NR[a]	17–65 s	[36, 42, 43, 82, 129]
VIPA spectrometer	0.3–2	460–621	8–10	0.05–10 s	[24, 34, 45, 60, 94, 99, 101, 103]
Line-scanning VIPA	0.6–1.6	250–500	9.8 to <20	~1 ms effective pixel time	[19, 21]
FTBM	~2	~1200	68–73	~25 µs effective pixel time	[20]
cw SBS	0.3–0.8	~39	<35	2–20 ms	[30, 136]
Pulsed SBS	0.49–0.57	102–151	7.7[b]	0.2–20 ms	[64, 66, 137]
BGM	~0.3	~100	N/A[c]	~0.1 ms	[67]
ISBS	7.6–150	2.5–6.4	NR[a]	0.02–10 ms	[51, 72–74]

Note: Values are representative of the cited implementations rather than intrinsic limits of each technique. Spectral precision denotes the standard deviation of repeated Brillouin-shift estimates where directly reported and is distinct from spectral resolution.
Abbreviations: BGM, brillouin gain microscopy; FTBM, fourier-transform brillouin microscopy; ISBS, impulsive stimulated brillouin scattering.
[a]NR, a directly comparable precision value was not reported under the conditions summarized here.
[b]The 7.7 MHz value was reported for a high-peak-power pulsed-SBS implementation at a 200 µs pixel time.
[c]BGM measures Brillouin gain at a selected mechanically contrasting frequency without acquiring a full spectrum at every pixel; a per-pixel Brillouin-shift precision is therefore not directly comparable.

[74]. These characteristics suggest that improving the Brillouin spatial resolution need not rely solely on increasing the numerical aperture. A further possibility is to introduce spatially selective suppression or depletion around the desired interaction region, conceptually analogous to depletion-based super-resolution strategies, so that peripheral Brillouin contributions are reduced while the central interaction is retained [138, 139]. Such an approach remains to be experimentally established for Brillouin microscopy, but it provides a possible route toward extending the effective mechanical resolution beyond that achieved by conventional focusing alone.

5.1.2 | *Imaging Speed and Spectral Quality*

The balance between these two aspects is particularly evident in spontaneous Brillouin systems(Figure 12d). Due to the weak scattering cross-section of spontaneous Brillouin, multiple acquisitions are generally necessary to obtain spectral information with a higher extinction ratio, which results in longer imaging times. Therefore, designing high-throughput systems is crucial for advancing the imaging performance of spontaneous Brillouin microscopy technology. This involves capturing more photons within the same integration time to achieve a sufficient signal-to-noise ratio with fewer acquisitions.

FP spectrometers face limitations regarding imaging speed. While integrating a VIPA can significantly improve imaging speed, it also reduces spectral resolution and extinction ratio compared to FP spectrometers. Innovative methods, such as the full-field Brillouin microscope, leverage an imaging Fourier transform spectrometer to significantly reduce the number of sampling points by utilizing the symmetry of the Brillouin spectrum, thus increasing imaging speed. However, the spectral precision of this approach is approximately 70 MHz, which is lower than that of some traditional methods, such as line-scanning Brillouin microscopy, which can achieve 20 MHz [19, 21].

When prior knowledge of the sample is available, stimulated Brillouin microscopy can eliminate the scanning step and detect specific frequencies. This approach, however, may result in the loss of specific signals, such as spectral linewidth [67]. Despite this, the introduction of angle detection from high numerical aperture (NA) system observations, along with the presence of multiple structures below the diffraction limit, suggests that detection at a single frequency can still provide spectral information beyond mere intensity, such as sample anisotropy. Moreover, impulsive stimulated Brillouin microscopy employs a broadband pulsed light source for excitation, generating multiple phonon modes without scanning. However, there is currently no unified method or established expression to quantify the spectral resolution of this technology. Some studies suggest that it is related to the measured spectral full width at half-maximum (FWHM), indicating that the detected sample influences spectral resolution [72]. Furthermore, the impact of changes in light weight across various frequencies, such as during pulse shaping, on spectral quality has not yet been thoroughly investigated.

5.1.3 | *Spatial Resolution and Spectral Quality*

Several factors influence the spatial resolution of Brillouin microscopy systems. In the current classical physical model (Figure 13a), although increasing the effective numerical aperture (NA) of the system can reduce the optical scattering volume in the sample, the phonon volume, determined by the phonon mean free path (the distance over which phonons can propagate), can lead to the expansion of the scattering region. The lateral component of the phonon mean free path contributes to improved lateral resolution. However, if the axial component exceeds the effective optical scattering volume, the detected signal will originate from damped sound waves, similar to the behavior observed in a truncated Bragg grating. This results in broadening the Brillouin spectrum, a phenomenon especially pronounced in isotropic samples

26999293, 2026, 11, Downloaded from https://advanced.onlinelibrary.wiley.com/doi/10.1002/adpr.202500132 by Emiliano Descrovi - ETH Zürich , Wiley Online Library on [06/11/2026]. See the Terms and Conditions (https://onlinelibrary.wiley.com/terms-and-conditions) on Wiley Online Library for rules of use; OA articles are governed by the applicable Creative Commons License

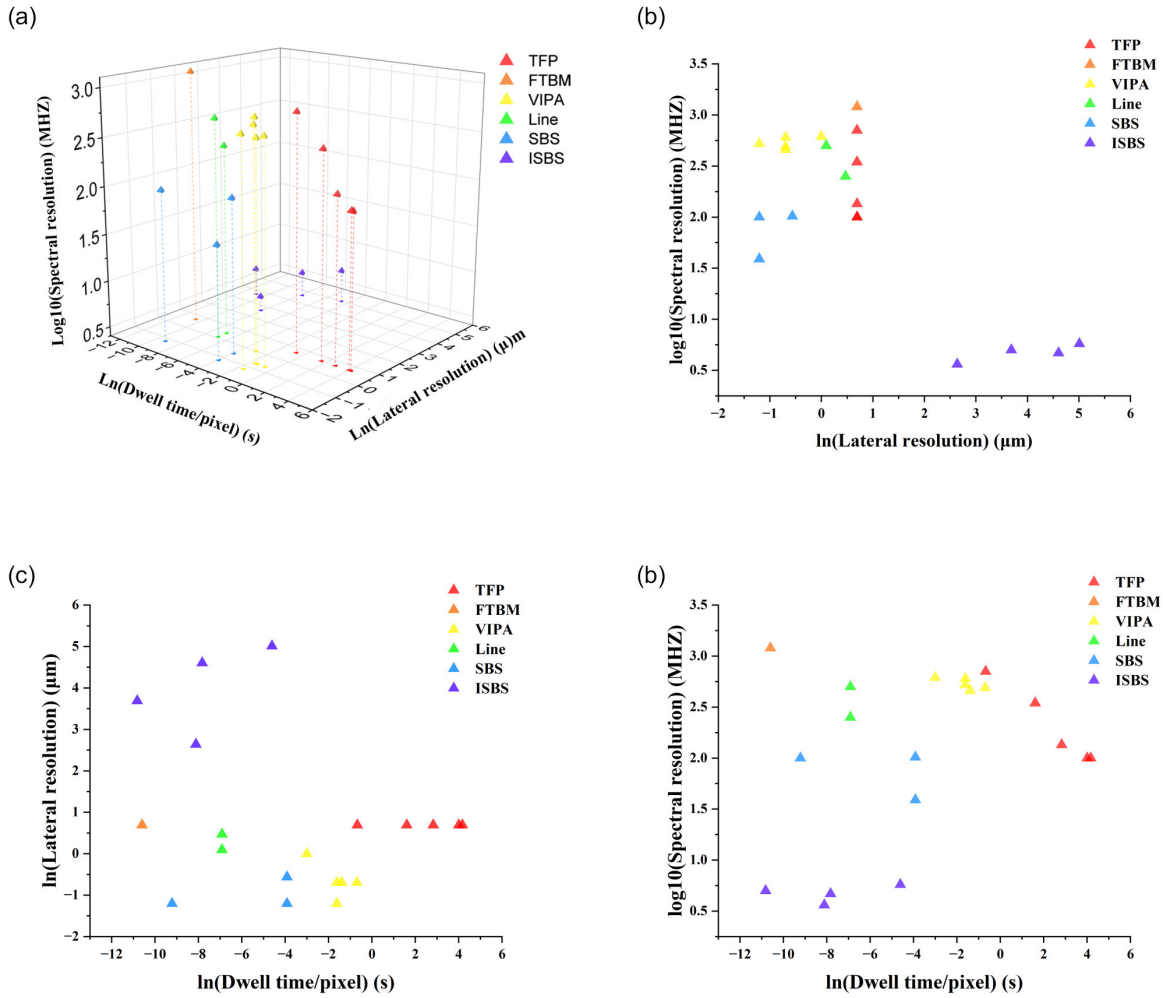


FIGURE 12 | Comparative visualization of imaging quality parameters across Brillouin microscopy experiments. (a) Imaging speed versus lateral resolution. (b) Spectral resolution versus lateral resolution. (c) Three-dimensional representation of three imaging performance parameters. (d) Imaging speed versus spectral resolution. Parameters are based on representative implementations of tandem Fabry–Perot (TFP) interferometry [42, 43, 54, 82, 129], VIPA-based Brillouin microscopy [34, 60, 99–101], line-scanning Brillouin microscopy [19, 21], Fourier-transform Brillouin microscopy (FTBM) [20], stimulated Brillouin scattering (SBS) microscopy [30, 64, 67], and impulsive stimulated Brillouin scattering (ISBS) microscopy [51, 71–73].

and at low-acoustic-mismatch structural boundaries [9, 138]. These factors not only influence spatial resolution but also significantly affect spectral quality. Prior to conducting further analysis, we hypothesize that the phonon volume and optical scattering volume jointly define an effective optoacoustic interaction range (Figure 13b), which is characterized by an effective dimension L_{eff}. As addressed in preceding sections, this parameter has been operationally defined through experimental validation [30]. Within this range, if the sample is ideally uniform and isotropic, increasing the effective NA of the system can improve both lateral and axial resolutions to some extent. However, this increase also introduces additional scattering wave vectors, leading to asymmetric broadening of the Brillouin spectrum, reduced peak values, and a shift to lower frequencies, as illustrated in Figure 13c. This effect is more pronounced in orthogonal scattering configurations. Although it has been theoretically proven that this phenomenon minimally impacts spectral quality within a specific NA range (NA < 0.7 for water or certain biological samples), it also limits further enhancements in spatial resolution [22, 25]. Additionally, if the sample is mechanically heterogeneous within this range ($L_{\text{eff}} > L_c$), denoted as L_c (the size of the uniformly mechanical structure), its influence must be considered. When L_c is much smaller than the acoustic wavelength Λ, the spectral information will reflect the average elastic properties of the components within that length range. Conversely, spectral information from various mechanical components will be collected when L_c is larger than the acoustic wavelength, as shown in Figure 13d (In the figure, Lpsf has been replaced with Leff in this article) [8]. This principle of balancing spatial resolution and spectral quality is applicable across nearly all Brillouin microscopy technologies. The mechanism that balances spatial resolution and spectral quality is widely relevant across different implementations of Brillouin microscopy technology. Based on Figure 12b and Table 1, it is clear that although the ISBS technique improves spectral resolution, it does so at the expense of spatial resolution.

As mentioned, before more advanced instruments are developed, various optical system designs will encounter trade-offs

26999293, 2026, 11, Downloaded from https://advanced.onlinelibrary.wiley.com/doi/10.1002/adpr.202500132 by Emiliano Descrovi - ETH Zürich , Wiley Online Library on [06/11/2026]. See the Terms and Conditions (https://onlinelibrary.wiley.com/terms-and-conditions) on Wiley Online Library for rules of use; OA articles are governed by the applicable Creative Commons License

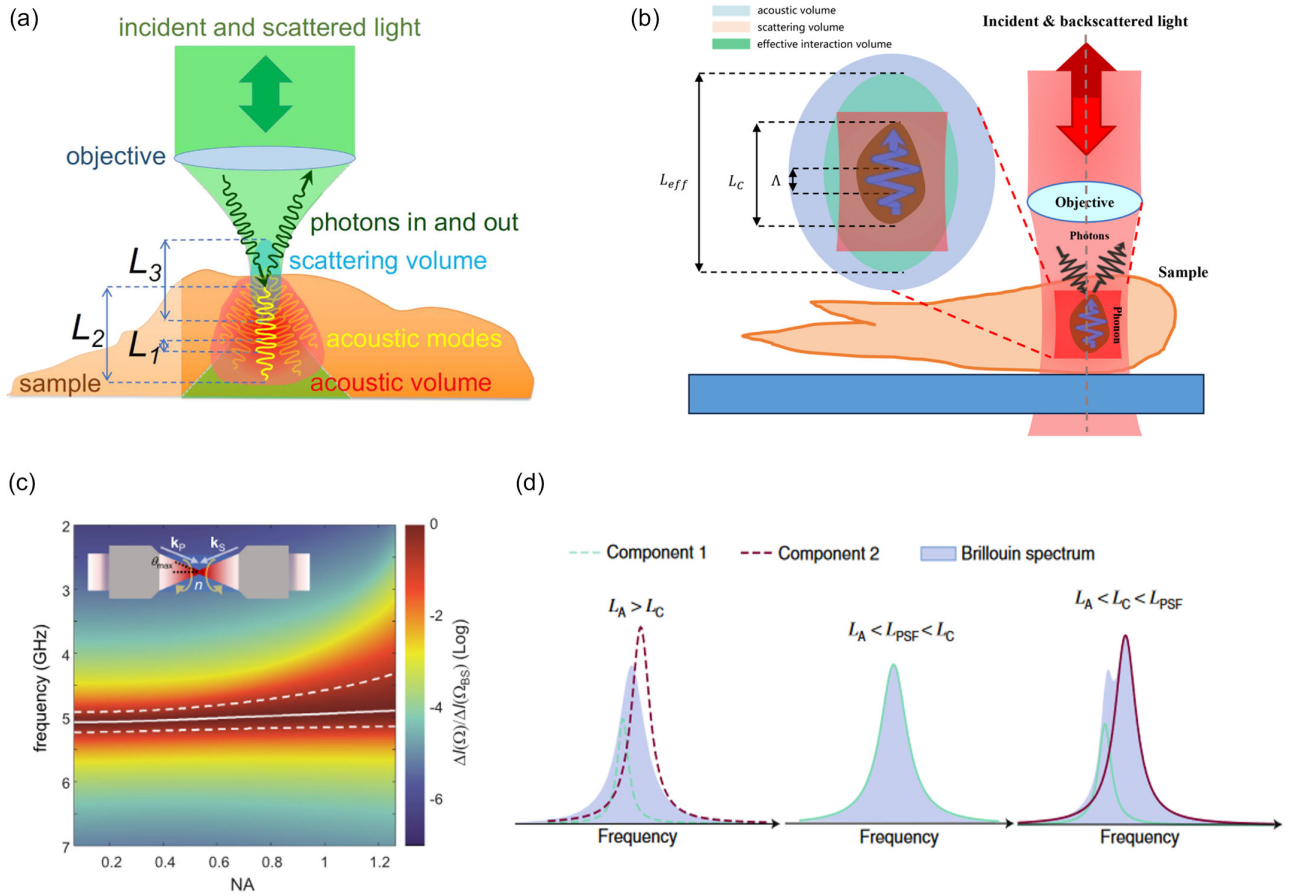


FIGURE 13 | (a) Micro-Brillouin scattering layout. L_1, L_2, and L_3 denote the characteristic dimensions of phonon wavelength, mean free path, and scattering volume, respectively. (b) Definition of the effective optoacoustic interaction range. (c) Dependence of the small-signal SBG spectrum of water on the focusing and collection NA (assumed to be identical) in SBS microscopy. (d) Depending on the relative size of the biological structure to the acoustic wavelength and the effective optoacoustic interaction length, individual components give rise to either an average (left), a unique (middle) or a sum (right) of their respective spectra. (a) Reproduced with permission [138]. Copyright 2020, American Chemical Society. (b) Adapted under the terms of the CC-BY Creative Commons Attribution 4.0 International license [10]. Copyright 2020, IOP Publishing Ltd. (c) Reproduced under the CC-BY Creative Commons Attribution 4.0 International license terms [25]. Copyright 2023, AIP Publishing (d) Reproduced with permission [8]. Copyright 2019, Springer Nature.

in their performance indicators. However, this isn't necessarily a negative aspect, as sufficient samples and application goals meet the required performance parameters. Additionally, the design methods for certain systems may see significant improvements due to advancements in instruments such as light sources, spectrometers, and acquisition devices. Any technique that enhances a single performance metric is worth investigating. For instance, the spatial resolution of impulsive stimulated Brillouin scattering can be improved by optimizing the magnification of the grating-4f system, which reduces the spatial range of interaction between the probe light and the transient grating. Traditional techniques, such as light field modulation technology, can also be utilized to compress the volume of the generated grating, thereby enhancing the system's spatial resolution, albeit at the cost of some gain. Moreover, as previously mentioned, one can improve the imaging speed of both stimulated and spontaneous Brillouin microscopy by accepting a lower spectral quality. With advancements in machine learning and optimization algorithms, it is now possible to fit the collected spectral information under more stringent conditions.

5.2 | Photodamage in Biomedical Imaging

Photodamage in Brillouin microscopy depends on wavelength, irradiance, exposure duration and temporal profile, focusing conditions, and the absorption and thermal-dissipation properties of the specimen. Because spontaneous Brillouin measurements are generally photon-limited, reducing optical power or acquisition time decreases the number of detected photons and can compromise signal-to-noise ratio and spectral precision. Stimulated implementations can shorten spectral acquisition but may require higher instantaneous or average optical powers. Optical exposure should therefore be evaluated together with the measurement precision and biological tolerance required for a specific experiment [140–142].

Multiplexed detection, pulsed excitation, and targeted spectral acquisition can redistribute the available photon budget and reduce the exposure required to obtain a given measurement, although their benefit depends on the spectral information that must be retained and on the optical sensitivity of the specimen [20, 64, 67, 73]. For live-cell and in vivo measurements, acceptable

26999293, 2026, 11, Downloaded from https://advanced.onlinelibrary.wiley.com/doi/10.1002/adpr.202500132 by Emiliano Descrovi - ETH Zürich , Wiley Online Library on [06/11/2026]. See the Terms and Conditions (https://onlinelibrary.wiley.com/terms-and-conditions) on Wiley Online Library for rules of use; OA articles are governed by the applicable Creative Commons License

exposure should therefore be established experimentally using sample-appropriate viability and physiological controls rather than a universal power threshold [140–142]. Brillouin microscopy has also been used to monitor mechanically relevant changes during photodynamic therapy, where optical irradiation is itself part of the treatment process [143].

TABLE 2 | Representative optical and exposure conditions reported for Brillouin microscopy in different samples.

Technology	Sample	Wavelength, nm	Effective NA/ geometry	Representative spatial resolution, μm^3	Power/ pulse energy at sample	Acquisition time	Reference
TFP interferometer	Lamellar bone	532	0.42	2×2×15	7 mW	55 s	[43]
TFP interferometer	Human collagen	532	0.42	2×2×10	10 mW	65 s	[129]
TFP interferometer	Primary human airway epithelial cells	660	1.0	1×1×–	<20 mW	20 s	[144]
VIPA spectrometer	CHO-K1 cells	532	1.42	0.5×0.5×~1	<4 mW	0.5 s	[99]
VIPA spectrometer	H6c7/ RWPE-1 organoid	780	0.65	1×1×6	15 mW	0.05 s	[60]
Two-stage VIPA	Myofibres/ arabidopsis; HeLa/U2OS	532	1.49	2×2×2	~7–10 mW/ ~5–6 mW	<1 s/ ≤100 ms	[24]
Two-stage VIPA	NIH 3T3 cells	532	0.60	~0.5×0.5×2	2–4 mW	0.1–0.2 s	[34]
Two-stage VIPA	Retina	660	0.42	1.8×1.8×10	11 mW	<0.2 s	[103]
Two-stage VIPA	Zebrafish	532	0.85	0.5×0.5×–	8.3 mW	0.25 s	[101]
Line-scanning VIPA	Tumour spheroid	780.24	0.1–0.3	1.6×1.6×4	340 mW	<200 ms	[19]
Line-scanning VIPA	Drosophila embryo	780	0.80	1.1×0.6×3.9	18–20 mW	<100 ms	[21]
FTBM	Zebrafish notochord	780	0.80	2×2×15	56 mW	100 ms	[20]
cw SBS	*C. elegans*	780.24	0.70	~0.3×0.3×2	265 mW	2–20 ms	[30]
Pulsed SBS	Fibroblast cell	780.24	0.70	0.57×0.55×2.58	<30 mW	20 ms	[64]
Pulsed SBS	HeLa cells	780.24	1.10	0.7×0.7×–	20 mW	20 ms	[66]
BGM	*C. elegans*	780	0.70	~0.3×0.3×2	228 mW	0.1 ms	[67]
ISBS	PDMS	Pump 532; probe 780	f1 = 150 mm; f2 = 60 mm; TG = 20.7 μm	13×14×160	Pump 13 μJ; probe 18 mW	<0.3 ms	[72]
ISBS	Hydrogel	Pump 532; probe 780	f1 = 150 mm; f2 = 125 mm; TG = 20.67 μm	100×100×100	Pump 60 μJ; probe 80 mW	<0.4 ms	[51]

Note: The values are sample- and implementation-specific operating conditions and should not be interpreted as intrinsic performance limits of the spectrometer type. A dash indicates that the corresponding dimension was not reported in the summarized source. For ISBS, pump pulse energy and continuous-wave probe power are listed separately. Abbreviation: TG, transient-grating period.

26999293, 2026, 11, Downloaded from https://advanced.onlinelibrary.wiley.com/doi/10.1002/adpr.202500132 by Emiliano Descrovi - ETH Zürich , Wiley Online Library on [06/11/2026]. See the Terms and Conditions (https://onlinelibrary.wiley.com/terms-and-conditions) on Wiley Online Library for rules of use; OA articles are governed by the applicable Creative Commons License

Representative optical and exposure conditions reported for different Brillouin implementations and samples are summarized in Table 2.

5.3 | Commercialization and Translational Challenges

Brillouin scattering microscopy is a promising technology known for its non-invasive nature, high spatial resolution, and precise detection capabilities regarding the mechanical properties of materials. It holds significant potential in biomedicine, materials science, and industrial testing. The transition of Brillouin microscopy from laboratory-built systems toward broader research and clinical use is limited by system complexity, alignment sensitivity, cost, calibration requirements, and the need for robust operation across different samples. These considerations are particularly important because many current implementations rely on specialized spectrometers, narrow-linewidth lasers, and custom filtering or stabilization modules. The high cost and specialized operation of current systems therefore remain practical barriers to their broader adoption.

Some studies are gradually addressing the challenges in imaging technology by focusing on critical aspects such as ease of use and portability. Research efforts to achieve fiber-integrated Brillouin imaging and chip-based laser filtering demonstrate that instrument innovation is the most effective path to miniaturization [77, 143]. However, these initiatives are still in their early stages and will require long cycles of iterative optimization before they become recognized and scalable products. At the same time, the system must support various application scenarios and functionalities. As the application section highlights, multimodal integration can target more specific samples for imaging analysis, providing richer and more accurate information. Brillouin microscopy can be categorized into three types: spontaneous, stimulated, and impulsive stimulated Brillouin microscopy, each with its own strengths in imaging performance suited for different applications. For example, spontaneous Brillouin microscopy allows for same-side detection and collection, making it ideal for in vivo observations of the cornea and similar structures. Stimulated Brillouin microscopy, limited by transmission observation techniques, delivers strong signals and high spectral resolution, making it suitable for ex vivo tissues or microbial samples. Despite having lower mechanical spatial resolution, Impulsive stimulated Brillouin technology offers fast imaging speeds that are advantageous for macroscopic rapid imaging scenarios. Therefore, designing a system that seamlessly switches between these three imaging modes could greatly enhance its versatility.

Another important consideration is the system's performance in turbid samples, which pose a common challenge in optical imaging. Multiple scattering can lead to spectral broadening and asymmetry, while the overall signal collected tends to attenuate, significantly degrading the quality of the images [65]. In general, long-wavelength light sources can be used to reduce the impact of tissue scattering and increase the penetration depth. Recently, a novel method has been proposed based on a birefringence-induced phase delay (BIPD) filter. This approach utilizes the anisotropy of birefringent crystals (such as YVO_4) to accumulate different phase delays for light of varying polarization states within the crystal. The wavelength differences between Brillouin-scattered light and Rayleigh-scattered light cause changes in their polarization states. Combining polarizers and liquid crystal retarders effectively filters out light from Rayleigh scattering (background light) while retaining Brillouin scattering. Compared to previous filtering strategies, this method enhances the throughput and signal-to-noise ratio, making the overall system design more compact [15, 57]. Meanwhile, we can draw inspiration from traditional imaging techniques, such as confocal or two-photon fluorescence imaging. For the current SBS and ISBS systems, an "aperture" can be designed in the spatial or frequency domain during signal collection to block non-conjugate returning signals, or additional thresholds and gates can be introduced in the excitation process (although the probe light also serves a localization function). Additionally, algorithm-assisted approaches—including computational imaging, deep learning, and integration with quantum imaging techniques—can help address the challenges of imaging in turbid media.

6 | Conclusions and Discussions

In summary, as the Brillouin microscopy technology continues to advance, its potential in the field of optical elastography will become increasingly evident. However, this progress will come with a series of complex and diverse challenges that require researchers to utilize the extensive resources of optical technologies to address effectively. At the core of Brillouin microscopy is Brillouin scattering, an inelastic scattering process that occurs when light interacts with either spontaneous or stimulated phonons in a material. This process exhibits a range of unique optical properties, offering multidimensional solutions and approaches that could lead to significant technological breakthroughs. Two key features of Brillouin scattering are the BLS frequency peak shift and the BLS linewidth, which are closely related to mechanical parameters such as the viscoelasticity of materials. These characteristics provide a high-precision data foundation for the quantitative analysis of the microstructure of biological tissues. Additionally, spectral resolution is a critical parameter that directly influences imaging quality measured under the diffraction limit. Optimizing the FWHM relies on advancements in light sources and improvements in detection system sensitivity. This can be achieved through the introduction of high-performance spectrometers or novel detectors that enhance the resolution capabilities. The application of nonlinear optical effects further extends the boundaries of this technology. These intrinsic mechanisms of optoacoustic interactions not only provide effective pathways for the direct measurement of mechanical parameters but also reveal tissue heterogeneity through the characteristics of acoustic wave propagation. This establishes a solid foundation for breakthroughs in super-resolution imaging, deep-tissue probing, and multi-parameter analysis.

The development potential of Brillouin microscopy is highlighted by its integration with other well-established optical microscopy technologies, which offer valuable resources for technical optimization. For instance, light field modulation techniques have made significant strides in the precise control of polarization, phase, and amplitude. Incorporating these techniques into Brillouin microscopy systems can greatly enhance optical

26999293, 2026, 11, Downloaded from https://advanced.onlinelibrary.wiley.com/doi/10.1002/adpr.202500132 by Emiliano Descrovi - ETH Zürich , Wiley Online Library on [06/11/2026]. See the Terms and Conditions (https://onlinelibrary.wiley.com/terms-and-conditions) on Wiley Online Library for rules of use; OA articles are governed by the applicable Creative Commons License

path stability and imaging contrast. Specifically, polarization modulation can effectively reduce Rayleigh scattering interference, phase modulation can improve beam focusing capabilities, and amplitude adjustment can optimize signal strength, all of which are essential for enhancing imaging quality in complex biological environments. Additionally, the rapid advancement of multivariate analysis techniques has revitalized Brillouin microscopy, potentially enabling hyperspectral imaging through algorithm optimization and data post-processing. The introduction of adaptive optics technology provides strong support for deep tissue imaging. By leveraging the inherent advantages of Brillouin microscopy—such as its label-free, non-contact nature and high-resolution detection of mechanical properties—along with its sensitivity to mechanical changes associated with hydration, it significantly enhances imaging quality through real-time correction of optical aberrations caused by biological tissues, thereby creating favorable conditions for deep-layer observations. Moreover, Brillouin microscopy can achieve multimodal integration with other optical imaging methods, such as fluorescence microscopy, Raman spectroscopy, or second-harmonic imaging. This allows for the synchronous acquisition of mechanical, biochemical, and structural information, creating a comprehensive analytical framework for biomedical research.

However, the future development of Brillouin microscopy is not without obstacles, and further progress will be accompanied by challenges and opportunities. By fully leveraging the optical properties inherent in Brillouin scattering, researchers can provide diverse approaches for technological breakthroughs. At the same time, integration with mature technologies such as light field modulation, computational imaging, and adaptive optics accelerates performance improvements and opens new pathways for its application in multimodal imaging. Although challenges such as light scattering limitations, viscoelastic separation, and standardization remain to be addressed, these very challenges provide rich exploration opportunities for the academic community. With the advancement of industrialization and the assistance of artificial intelligence, Brillouin microscopy is expected to transition from laboratory research to clinical applications, ultimately bringing revolutionary changes to precision medicine and regenerative medicine. The development of this technology not only demonstrates the immense potential of optical technologies in biomechanical research and establishes a broad platform for interdisciplinary collaboration, deserving the dedication of more researchers to drive its realization of greater academic and societal value collectively.

Author Contributions

X.L., Q.Y. and F.L.: provided some guidance on image processing and formatting. K.T.: wrote the manuscript. X.Y., E.D., K.T. and F.L.: conceived and supervised the project.

Funding

Financial support was provided by the National Key Research and Development Program of China (Grant No. 2022ZD0119401), National Natural Science Foundation of China (Grant Nos. T2293751, T2293750 and 92250304), National Key Research and Development Program of China (Grant Nos. 2024YFF1206700, 2024YFF1206701 and 2024YFF1206705).

Conflicts of Interest

The authors declare no conflicts of interest.

Data Availability Statement

The data that support the findings of this study are available from the corresponding author upon reasonable request.

References

1. F. Palombo and D. Fioretto, "Brillouin Light Scattering: Applications in Biomedical Sciences," *Chemical Reviews* 119, no. 13 (2019): 7833–7847, https://doi.org/10.1021/acs.chemrev.9b00019.

2. I. Kabakova, J. Zhang, Y. Xiang, et al., "Brillouin Microscopy," *Nature Reviews Methods Primers* 4, no. 1 (2024): 8, https://doi.org/10.1038/s43586-023-00286-z.

3. P. Bouvet, C. Bevilacqua, Y. Ambekar, et al., "Consensus Statement on Brillouin Light Scattering Microscopy of Biological Materials," *Nature Photonics* 19, no. 7 (2025): 681–691, https://doi.org/10.1038/s41566-025-01681-6.

4. K. J. Koski and J. L. Yarger, "Brillouin Imaging," *Applied Physics Letters* 87, no. 6 (2005): 061903, https://doi.org/10.1063/1.1999857.

5. G. Scarcelli and S. H. Yun, "Confocal Brillouin Microscopy for Three-Dimensional Mechanical Imaging," *Nature Photonics* 2 (2007): 39–43, https://doi.org/10.1038/nphoton.2007.250.

6. C. W. Ballmann, J. V. Thompson, A. J. Traverso, Z. Meng, M. O. Scully, and V. V. Yakovlev, "Stimulated Brillouin Scattering Microscopic Imaging," *Scientific Reports* 5, no. 1 (2015): 18139, https://doi.org/10.1038/srep18139.

7. C. W. Ballmann, Z. Meng, A. J. Traverso, M. O. Scully, and V. V. Yakovlev, "Impulsive Brillouin Microscopy," *Optica* 4, no. 1 (2017): 124, https://doi.org/10.1364/OPTICA.4.000124.

8. R. Prevedel, A. Diz-Muñoz, G. Ruocco, and G. Antonacci, "Brillouin Microscopy: An Emerging Tool for Mechanobiology," *Nature Methods* 16, no. 10 (2019): 969–977, https://doi.org/10.1038/s41592-019-0543-3.

9. G. Antonacci, T. Beck, A. Bilenca, et al., "Recent Progress and Current Opinions in Brillouin Microscopy for Life Science Applications," *Biophysical Reviews* 12, no. 3 (2020): 615–624, https://doi.org/10.1007/s12551-020-00701-9.

10. C. Poon, J. Chou, M. Cortie, and I. Kabakova, "Brillouin Imaging for Studies of Micromechanics in Biology and Biomedicine: From Current State-of-the-Art to Future Clinical Translation," *Journal of Physics: Photonics* 3, no. 1 (2020): 012002, https://doi.org/10.1088/2515-7647/abbf8c.

11. C. Shi, H. Zhang, and J. Zhang, "Non-Contact and Label-Free Biomechanical Imaging: Stimulated Brillouin Microscopy and Beyond," *Frontiers in Physics* 11 (2023): 1175653, https://doi.org/10.3389/fphy.2023.1175653.

12. A. Bilenca, R. Prevedel, and G. Scarcelli, "Current State of Stimulated Brillouin Scattering Microscopy for the Life Sciences," *Journal of Physics: Photonics* 6, no. 3 (2024): 032001, https://doi.org/10.1088/2515-7647/ad5506.

13. N. Falkner, M.-N. Duman, Z. Zabolizadeh, et al., "Brillouin Microscopy in Cancer Research: A Review," *Journal of Biomedical Optics* 30, no. 12 (2025): 1–17, https://doi.org/10.1117/1.JBO.30.12.124509.

14. J. Zhang and G. Scarcelli, "Mapping Mechanical Properties of Biological Materials via an Add-on Brillouin Module to Confocal Microscopes," *Nature Protocols* 16, no. 2 (2021): 1251–1275, https://doi.org/10.1038/s41596-020-00457-2.

26999293, 2026, 11, Downloaded from https://advanced.onlinelibrary.wiley.com/doi/10.1002/adpr.202500132 by Emiliano Descrovi - ETH Zürich , Wiley Online Library on [06/11/2026]. See the Terms and Conditions (https://onlinelibrary.wiley.com/terms-and-conditions) on Wiley Online Library for rules of use; OA articles are governed by the applicable Creative Commons License

15. A. Fiore, J. Zhang, P. Shao, S. H. Yun, and G. Scarcelli, "High-Extinction Virtually Imaged Phased Array-Based Brillouin Spectroscopy of Turbid Biological Media," *Applied Physics Letters* 108, no. 20 (2016): 203701, https://doi.org/10.1063/1.4948353.

16. G. Antonacci, "Dark-Field Brillouin Microscopy," *Optics Letters* 42, no. 7 (2017): 1432, https://doi.org/10.1364/OL.42.001432.

17. A. Fiore and G. Scarcelli, "Single, Etalon Design for Two-Stage Cross-Axis VIPA Spectroscopy," *Biomedical Optics Express* 10, no. 3 (2019): 1475, https://doi.org/10.1364/BOE.10.001475.

18. J. Zhang, A. Fiore, S.-H. Yun, H. Kim, and G. Scarcelli, "Line-Scanning Brillouin Microscopy for Rapid Non-Invasive Mechanical Imaging," *Scientific Reports* 6, no. 1 (2016): 35398, https://doi.org/10.1038/srep35398.

19. J. Zhang, M. Nikolic, K. Tanner, and G. Scarcelli, "Rapid Biomechanical Imaging at Low Irradiation Level via Dual Line-Scanning Brillouin Microscopy," *Nature Methods* 20, no. 5 (2023): 677–681, https://doi.org/10.1038/s41592-023-01816-z.

20. C. Bevilacqua and R. Prevedel, "Full-Field Brillouin Microscopy Based on an Imaging Fourier-Transform Spectrometer," *Nature Photonics* 19, no. 5 (2025): 494–501, https://doi.org/10.1038/s41566-025-01619-y.

21. C. Bevilacqua, J. M. Gomez, U.-M. Fiuza, et al., "High-Resolution Line-Scan Brillouin Microscopy for Live Imaging of Mechanical Properties During Embryo Development," *Nature Methods* 20, no. 5 (2023): 755–760, https://doi.org/10.1038/s41592-023-01822-1.

22. G. Antonacci, M. R. Foreman, C. Paterson, and P. Török, "Spectral Broadening in Brillouin Imaging," *Applied Physics Letters* 103, no. 22 (2013): 221105, https://doi.org/10.1063/1.4836477.

23. A. M. Eltony, P. Shao, and S.-H. Yun, "Measuring Mechanical Anisotropy of the Cornea With Brillouin Microscopy," *Nature Communications* 13, no. 1 (2022): 1354, https://doi.org/10.1038/s41467-022-29038-5.

24. H. Keshmiri, D. Cikes, M. Samalova, et al., "Brillouin Light Scattering Anisotropy Microscopy for Imaging the Viscoelastic Anisotropy in Living Cells," *Nature Photonics* 18, no. 3 (2024): 276–285, https://doi.org/10.1038/s41566-023-01368-w.

25. R. Shaashoua and A. Bilenca, "Aperture-Induced Spectral Effects in Stimulated Brillouin Scattering Microscopy," *Applied Physics Letters* 122, no. 14 (2023): 143702, https://doi.org/10.1063/5.0146627.

26. E. Gross, "Change of Wave-Length of Light due to Elastic Heat Waves at Scattering in Liquids," *Nature* 126, no. 3171 (1930): 201–202, https://doi.org/10.1038/126201a0.

27. S. Kojima, "100th Anniversary of Brillouin Scattering: Impact on Materials Science," *Materials* 15, no. 10 (2022): 3518, https://doi.org/10.3390/ma15103518.

28. I. L. Fabelinskii, *Molecular Scattering of Light* (Springer New York, 1968), https://doi.org/10.1007/978-1-4684-1740-1.

29. R. Y. Chiao, C. H. Townes, and B. P. Stoicheff, "Stimulated Brillouin Scattering and Coherent Generation of Intense Hypersonic Waves," *Physical Review Letters* 12, no. 21 (1964): 592–595, https://doi.org/10.1103/PhysRevLett.12.592.

30. I. Remer, R. Shaashoua, N. Shemesh, A. Ben-Zvi, and A. Bilenca, "High-Sensitivity and High-Specificity Biomechanical Imaging by Stimulated Brillouin Scattering Microscopy," *Nature Methods* 17, no. 9 (2020): 913–916, https://doi.org/10.1038/s41592-020-0882-0.

31. B. Krug, N. Koukourakis, and J. W. Czarske, "Impulsive Stimulated Brillouin Microscopy for Non-Contact, Fast Mechanical Investigations of Hydrogels," *Optics Express* 27, no. 19 (2019): 26910, https://doi.org/10.1364/OE.27.026910.

32. T. Li, F. Li, X. Liu, V. V. Yakovlev, and G. S. Agarwal, "Quantum-Enhanced Stimulated Brillouin Scattering Spectroscopy and Imaging," *Optica* 9, no. 8 (2022): 959, https://doi.org/10.1364/OPTICA.467635.

33. R. Schlüßler, S. Möllmert, S. Abuhattum, et al., "Mechanical Mapping of Spinal Cord Growth and Repair in Living Zebrafish Larvae by Brillouin Imaging," *Biophysical Journal* 115, no. 5 (2018): 911–923, https://doi.org/10.1016/j.bpj.2018.07.027.

34. G. Scarcelli, W. J. Polacheck, H. T. Nia, et al., "Noncontact Three-Dimensional Mapping of Intracellular Hydromechanical Properties by Brillouin Microscopy," *Nature Methods* 12, no. 12 (2015): 1132–1134, https://doi.org/10.1038/nmeth.3616.

35. S. Mattana, M. Mattarelli, L. Urbanelli, et al., "Non-Contact Mechanical and Chemical Analysis of Single Living Cells by Microspectroscopic Techniques," *Light: Science & Applications* 7, no. 2 (2017): 17139–17139, https://doi.org/10.1038/lsa.2017.139.

36. Z. Coker, M. Troyanova-Wood, A. J. Traverso, T. Yakupov, Z. N. Utegulov, and V. V. Yakovlev, "Assessing Performance of Modern Brillouin Spectrometers," *Optics Express* 26, no. 3 (2018): 2400, https://doi.org/10.1364/OE.26.002400.

37. A. Fiore, C. Bevilacqua, and G. Scarcelli, "Direct Three-Dimensional Measurement of Refractive Index via Dual Photon-Phonon Scattering," *Physical Review Letters* 122, no. 10 (2019): 103901, https://doi.org/10.1103/PhysRevLett.122.103901.

38. S. Abuhattum, K. Kim, T. M. Franzmann, et al., "Intracellular Mass Density Increase Is Accompanying but Not Sufficient for Stiffening and Growth Arrest of Yeast Cells," *Frontiers in Physics* 6 (2018): 131, https://doi.org/10.3389/fphy.2018.00131.

39. G. Popescu, Y. Park, N. Lue, et al., "Optical Imaging of Cell Mass and Growth Dynamics," *American Journal of Physiology-Cell Physiology* 295, no. 2 (2008): C538–C544, https://doi.org/10.1152/ajpcell.00121.2008.

40. R. Schlüßler, K. Kim, M. Nötzel, et al., "Correlative All-Optical Quantification of Mass Density and Mechanics of Subcellular Compartments With Fluorescence Specificity," *eLife* 11 (2022): e68490, https://doi.org/10.7554/eLife.68490.

41. T. Beck, L.-M. Van Der Linden, W. M. Borcherds, et al., "Optical Characterization of Molecular Interaction Strength in Protein Condensates," *Molecular Biology of the Cell* 35, no. 12 (2024): ar154, https://doi.org/10.1091/mbc.E24-03-0128.

42. M. Bailey, M. Alunni-Cardinali, N. Correa, et al., "Viscoelastic Properties of Biopolymer Hydrogels Determined by Brillouin Spectroscopy: A Probe of Tissue Micromechanics," *Science Advances* 6, no. 44 (2020): eabc1937, https://doi.org/10.1126/sciadv.abc1937.

43. M. Alunni Cardinali, A. Di Michele, M. Mattarelli, et al., "Brillouin–Raman Microspectroscopy for the Morpho-Mechanical Imaging of Human Lamellar Bone," *Journal of the Royal Society Interface* 19, no. 187 (2022): 20210642, https://doi.org/10.1098/rsif.2021.0642.

44. S. Oh, C. Lee, W. Yang, et al., "Protein and Lipid Mass Concentration Measurement in Tissues by Stimulated Raman Scattering Microscopy," *Proceedings of the National Academy of Sciences* 119, no. 17 (2022): e2117938119, https://doi.org/10.1073/pnas.2117938119.

45. C. Testi, E. Pontecorvo, C. Bartoli, et al., "Stabilized Real-Time Brillouin Microscopy Reveals Fractal Organization of Protein Condensates in Living Cells," *Nature Communications* 17, no. 1 (2026): 2387, https://doi.org/10.1038/s41467-026-68984-2.

46. Y. Xiang, M. R. Foreman, and P. Török, "SNR Enhancement in Brillouin Microspectroscopy Using Spectrum Reconstruction," *Biomedical Optics Express* 11, no. 2 (2020): 1020, https://doi.org/10.1364/BOE.380798.

47. R. Shaashoua, T. Levy, B. Rotblat, and A. Bilenca, "Enhancing Mechanical Stimulated Brillouin Scattering Imaging With Physics-Driven Model Selection," *Laser & Photonics Reviews* 18, no. 6 (2024): 2301054, https://doi.org/10.1002/lpor.202301054.

48. K. Elsayad, "Spectral Phasor Analysis for Brillouin Microspectroscopy," *Frontiers in Physics* 7 (2019): 62, https://doi.org/10.3389/fphy.2019.00062.

26999293, 2026, 11, Downloaded from https://advanced.onlinelibrary.wiley.com/doi/10.1002/adpr.202500132 by Emiliano Descrovi - ETH Zürich , Wiley Online Library on [06/11/2026]. See the Terms and Conditions (https://onlinelibrary.wiley.com/terms-and-conditions) on Wiley Online Library for rules of use; OA articles are governed by the applicable Creative Commons License

49. D. Fioretto, S. Caponi, and F. Palombo, "Brillouin-Raman Mapping of Natural Fibers With Spectral Moment Analysis," *Biomedical Optics Express* 10, no. 3 (2019): 1469, https://doi.org/10.1364/BOE.10.001469.

50. F. Palombo, F. Masia, S. Mattana, et al., "Hyperspectral Analysis Applied to Micro-Brillouin Maps of Amyloid-Beta Plaques in Alzheimer's Disease Brains," *The Analyst* 143, no. 24 (2018): 6095–6102, https://doi.org/10.1039/C8AN01291A.

51. J. Li, H. Zhang, M. Lu, H. Wei, and Y. Li, "Sensitive Impulsive Stimulated Brillouin Spectroscopy by an Adaptive Noise-Suppression Matrix Pencil," *Optics Express* 30, no. 16 (2022): 29598, https://doi.org/10.1364/OE.465106.

52. Y. Xiang, K. L. C. Seow, C. Paterson, and P. Török, "Multivariate Analysis of Brillouin Imaging Data by Supervised and Unsupervised Learning," *Journal of Biophotonics* 14, no. 7 (2021): e202000508, https://doi.org/10.1002/jbio.202000508.

53. H. Mahmodi, C. G. Poulton, M. N. Leslie, et al., "Principal Component Analysis in Application to Brillouin Microscopy Data," *Journal of Physics: Photonics* 6, no. 2 (2024): 025009, https://doi.org/10.1088/2515-7647/ad369d.

54. F. Scarponi, S. Mattana, S. Corezzi, et al., "High-Performance Versatile Setup for Simultaneous Brillouin-Raman Microspectroscopy," *Physical Review X* 7, no. 3 (2017): 031015, https://doi.org/10.1103/PhysRevX.7.031015.

55. G. Antonacci, G. Lepert, C. Paterson, and P. Török, "Elastic Suppression in Brillouin Imaging by Destructive Interference," *Applied Physics Letters* 107, no. 6 (2015): 061102, https://doi.org/10.1063/1.4927400.

56. G. Scarcelli and S. H. Yun, "Multistage VIPA, Etalons for High-Extinction Parallel Brillouin Spectroscopy," *Optics Express* 19, no. 11 (2011): 10913, https://doi.org/10.1364/OE.19.010913.

57. P. Shao, S. Besner, J. Zhang, G. Scarcelli, and S.-H. Yun, "Etalon Filters for Brillouin Microscopy of Highly Scattering Tissues," *Optics Express* 24, no. 19 (2016): 22232, https://doi.org/10.1364/OE.24.022232.

58. E. Edrei, M. C. Gather, and G. Scarcelli, "Integration of Spectral Coronagraphy Within VIPA-Based Spectrometers for High Extinction Brillouin Imaging," *Optics Express* 25, no. 6 (2017): 6895, https://doi.org/10.1364/OE.25.006895.

59. C. Pang, J. Shi, F. Peng, et al., "Vortex-Structured-Light-Assisted High-Contrast Brillouin Spectroscopy," *ACS Photonics* 13, no. 5 (2026): 1511–1518, https://doi.org/10.1021/acsphotonics.5c02933.

60. P. Bouvet, F. Clément, A. Papoz, T. Dehoux, and J.-C. Baritaux, "Multimode Fiber-Coupled VIPA Spectrometer for High-Throughput Brillouin Imaging of Biological Samples," *Journal of Physics: Photonics* 6, no. 2 (2024): 025010, https://doi.org/10.1088/2515-7647/ad378c.

61. R. Hutchins, G. Zanini, and G. Scarcelli, "Full-Field Optical Spectroscopy at a High Spectral Resolution Using Atomic Vapors," *Optics Express* 31, no. 3 (2023): 4334, https://doi.org/10.1364/OE.479253.

62. J. R. Rosvold, J. B. Murray, G. Zanini, B. Redding, and G. Scarcelli, "Impact of Polarization Pulling on Optimal Spectrometer Design for Stimulated Brillouin Scattering Microscopy," *APL Photonics* 9, no. 10 (2024): 100807, https://doi.org/10.1063/5.0225074.

63. M. A. Taylor, A. W. Kijas, Z. Wang, J. Lauko, and A. E. Rowan, "Heterodyne Brillouin Microscopy for Biomechanical Imaging," *Biomedical Optics Express* 12, no. 10 (2021): 6259, https://doi.org/10.1364/BOE.435869.

64. F. Yang, C. Bevilacqua, S. Hambura, et al., "Pulsed Stimulated Brillouin Microscopy Enables High-Sensitivity Mechanical Imaging of Live and Fragile Biological Specimens," *Nature Methods* 20, no. 12 (2023): 1971–1979, https://doi.org/10.1038/s41592-023-02054-z.

65. I. Remer and A. Bilenca, "High-Speed Stimulated Brillouin Scattering Spectroscopy at 780 nm," *APL Photonics* 1, no. 6 (2016): 061301, https://doi.org/10.1063/1.4953620.

66. D. M. Chow and S.-H. Yun, "Pulsed Stimulated Brillouin Microscopy," *Optics Express* 31, no. 12 (2023): 19818, https://doi.org/10.1364/OE.489158.

67. R. Shaashoua, L. Kasuker, M. Kishner, et al., "Brillouin Gain Microscopy," *Nature Photonics* 18, no. 8 (2024): 836–841, https://doi.org/10.1038/s41566-024-01445-8.

68. T. Li, V. Cheburkanov, V. V. Yakovlev, G. S. Agarwal, and M. O. Scully, "Harnessing Quantum Light for Microscopic Biomechanical Imaging of Cells and Tissues," *Proceedings of the National Academy of Sciences* 121, no. 45 (2024): e2413938121, https://doi.org/10.1073/pnas.2413938121.

69. T. Le, J. Li, H. Wei, and Y. Li, "Speed of Sound Measurement and Mapping in Transparent Materials by Impulsive Stimulated Brillouin Microscopy," *Journal of Physics: Photonics* 6, no. 3 (2024): 035004, https://doi.org/10.1088/2515-7647/ad46a8.

70. B. Krug, N. Koukourakis, J. Guck, and J. Czarske, "Nonlinear Microscopy Using Impulsive Stimulated Brillouin Scattering for High-Speed Elastography," *Optics Express* 30, no. 4 (2022): 4748, https://doi.org/10.1364/OE.449980.

71. J. Li, H. Zhang, X. Chen, T. Le, H. Wei, and Y. Li, "High-Speed Non-Contact Measurement of Elasto-Optic Coefficient via Laser-Induced Phonons," *Applied Physics Letters* 121, no. 25 (2022): 251102, https://doi.org/10.1063/5.0134976.

72. J. Li, T. Le, H. Zhang, H. Wei, and Y. Li, "High-Speed Impulsive Stimulated Brillouin Microscopy," *Photonics Research* 12, no. 4 (2024): 730, https://doi.org/10.1364/PRJ.509922.

73. D. Krause, L. Liebig, J. Boehm, N. Koukourakis, and J. W. Czarske, "Single-Shot Impulsive Stimulated Brillouin Microscopy by Tailored Ultrashort Pulses," *Journal of the European Optical Society-Rapid Publications* 21, no. 1 (2025): 9, https://doi.org/10.1051/jeos/2025004.

74. S. P. O'Connor, D. A. Doktor, M. O. Scully, and V. V. Yakovlev, "Spectral Resolution Enhancement for Impulsive Stimulated Brillouin Spectroscopy by Expanding Pump Beam Geometry," *Optics Express* 31, no. 9 (2023): 14604, https://doi.org/10.1364/OE.487131.

75. T. Le, J. Li, H. Wei, and Y. Li, "Improvement of Gain and Spatial Resolution for Impulsive Stimulated Brillouin Scattering Microscopy," *Photoacoustics* 42 (2025): 100696, https://doi.org/10.1016/j.pacs.2025.100696.

76. M. Mattarelli, G. Capponi, A. A. Passeri, D. Fioretto, and S. Caponi, "Disentanglement of Multiple Scattering Contribution in Brillouin Microscopy," *ACS Photonics* 9, no. 6 (2022): 2087–2091, https://doi.org/10.1021/acsphotonics.2c00322.

77. G. Antonacci, R. Vanna, M. Ventura, et al., "Birefringence-Induced Phase Delay Enables Brillouin Mechanical Imaging in Turbid Media," *Nature Communications* 15, no. 1 (2024): 5202, https://doi.org/10.1038/s41467-024-49419-2.

78. T. Vasileiadis, M. Schöttle, M. Theis, M. Retsch, G. Fytas, and B. Graczykowski, "Elasticity Mapping of Colloidal Glasses Reveals the Interplay Between Mesoscopic Order and Granular Mechanics," *Small Methods* 9, no. 3 (2025): 2400855, https://doi.org/10.1002/smtd.202400855.

79. M. Philipp, U. Müller, R. Sanctuary, et al., "Heterogeneous Transport Processes and Unexpected Structure Formation in Layered Epoxy and Epoxy-Alumina Nanocomposite Systems," *Journal of Adhesion* 87, no. 11 (2011): 1073–1098, https://doi.org/10.1080/00218464.2011.609448.

80. M. Philipp, U. Müller, R. Sanctuary, J. Kieffer, W. Possart, and J. K. Krüger, "On the Interplay Between Matter Transport and Structure Formation at Epoxy–Hardener Interfaces Visualized by Scanning Brillouin Microscopy," *Soft Matter* 7, no. 1 (2011): 118–124, https://doi.org/10.1039/C0SM00505C.

81. R. Sanctuary, M. Philipp, U. Müller, W. Possart, R. Jiménez-Riobóo, and J. K. Krüger, "Space and Time Resolving Molecular Acoustics as a

26999293, 2026, 11, Downloaded from https://advanced.onlinelibrary.wiley.com/doi/10.1002/adpr.202500132 by Emiliano Descrovi - ETH Zürich , Wiley Online Library on [06/11/2026]. See the Terms and Conditions (https://onlinelibrary.wiley.com/terms-and-conditions) on Wiley Online Library for rules of use; OA articles are governed by the applicable Creative Commons License

Tool to Visualize Epoxy Formation at a Planar Hardener–Resin Interface," *Chemical Physics Letters* 476, no. 1–3 (2009): 11–14, https://doi.org/10.1016/j.cplett.2009.05.076.

82. H. Mahmodi, A. Piloni, R. H. Utama, and I. Kabakova, "Mechanical Mapping of Bioprinted Hydrogel Models by Brillouin Microscopy," *Bioprinting* 23 (2021): e00151, https://doi.org/10.1016/j.bprint.2021.e00151.

83. Z. Meng, T. Thakur, C. Chitrakar, M. K. Jaiswal, A. K. Gaharwar, and V. V. Yakovlev, "Assessment of Local Heterogeneity in Mechanical Properties of Nanostructured Hydrogel Networks," *ACS Nano* 11, no. 8 (2017): 7690–7696, https://doi.org/10.1021/acsnano.6b08526.

84. L. Polonchuk, L. Surija, M. H. Lee, et al., "Towards Engineering Heart Tissues From Bioprinted Cardiac Spheroids," *Biofabrication* 13, no. 4 (2021): 045009, https://doi.org/10.1088/1758-5090/ac14ca.

85. M. A. Rad, H. Mahmodi, E. C. Filipe, T. R. Cox, I. Kabakova, and J. L. Tipper, "Micromechanical Characterisation of 3D Bioprinted Neural Cell Models Using Brillouin Microspectroscopy," *Bioprinting* 25 (2022): e00179, https://doi.org/10.1016/j.bprint.2021.e00179.

86. O. Wojewoda, M. Hrtoň, M. Dhankhar, et al., "Phase-Resolved Optical Characterization of Nanoscale Spin Waves," *Applied Physics Letters* 122, no. 20 (2023): 202405, https://doi.org/10.1063/5.0151338.

87. M. Lejman, G. Vaudel, V. Juvé, et al., "*In Situ* Determination of the Optical Axis Orientation in a Single Grain Using Time-Domain Brillouin Microscopy," *Applied Physics Letters* 126, no. 1 (2025): 012201, https://doi.org/10.1063/5.0245340.

88. B. Vincent, J. K. Krüger, O. Elmazria, et al., "Imaging of Microwave-Induced Acoustic Fields in $LiNbO_3$ by High-Performance Brillouin Microscopy," *Journal of Physics D: Applied Physics* 38, no. 12 (2005): 2026–2030, https://doi.org/10.1088/0022-3727/38/12/026.

89. Z. Zhang, M. Vogel, J. Holanda, et al., "Spin-Wave Frequency Division Multiplexing in an Yttrium Iron Garnet Microstripe Magnetized by Inhomogeneous Field," *Applied Physics Letters* 115, no. 23 (2019): 232402, https://doi.org/10.1063/1.5127881.

90. J. Ding, V. E. Demidov, M. G. Cottam, S. O. Demokritov, and A. O. Adeyeye, "Dynamic Behavior of $Ni_{80}Fe_{20}$ Nanowires With Controlled Defects," *Applied Physics Letters* 104, no. 14 (2014): 143105, https://doi.org/10.1063/1.4870837.

91. V. E. Gusev and P. Ruello, "Advances in Applications of Time-Domain Brillouin Scattering for Nanoscale Imaging," *Applied Physics Reviews* 5, no. 3 (2018): 031101, https://doi.org/10.1063/1.5017241.

92. M. B. Jungfleisch, W. Zhang, W. Jiang, et al., "Spin Waves in Micro-Structured Yttrium Iron Garnet Nanometer-Thick Films," *Journal of Applied Physics* 117, no. 17 (2015): 17D128, https://doi.org/10.1063/1.4916027.

93. T. Landes, B. P. Khanal, H. L. Bethge, et al., "Micromechanical Behavior of the Apple Fruit Cuticle Investigated by Brillouin Light Scattering Microscopy," *Communications Biology* 8, no. 1 (2025): 174, https://doi.org/10.1038/s42003-025-07555-5.

94. J. Zhang, F. Alisafaei, M. Nikolić, et al., "Nuclear Mechanics Within Intact Cells Is Regulated by Cytoskeletal Network and Internal Nanostructures," *Small* 16, no. 18 (2020): 1907688, https://doi.org/10.1002/smll.201907688.

95. A. A. Passeri, C. Argentati, F. Morena, et al., "Brillouin Spectroscopy for Accurate Assessment of Morphological and Mechanical Characteristics in Micro-Structured Samples," *Journal of Physics: Photonics* 6, no. 3 (2024): 035016, https://doi.org/10.1088/2515-7647/ad50b2.

96. G. Antonacci and S. Braakman, "Biomechanics of Subcellular Structures by Non-Invasive Brillouin Microscopy," *Scientific Reports* 6, no. 1 (2016): 37217, https://doi.org/10.1038/srep37217.

97. S. Coppola, T. Schmidt, G. Ruocco, and G. Antonacci, "Quantifying Cellular Forces and Biomechanical Properties by Correlative Micropillar Traction Force and Brillouin Microscopy," *Biomedical Optics Express* 10, no. 5 (2019): 2202, https://doi.org/10.1364/BOE.10.002202.

98. E. Frittoli, A. Palamidessi, F. Iannelli, et al., "Tissue Fluidification Promotes a cGAS–STING Cytosolic DNA Response in Invasive Breast Cancer," *Nature Materials* 22, no. 5 (2023): 644–655, https://doi.org/10.1038/s41563-022-01431-x.

99. Z. N. Coker, M. Troyanova-Wood, Z. A. Steelman, et al., "Brillouin Microscopy Monitors Rapid Responses in Subcellular Compartments," *PhotoniX* 5, no. 1 (2024): 9, https://doi.org/10.1186/s43074-024-00123-w.

100. C. J. Chan, C. Bevilacqua, and R. Prevedel, "Mechanical Mapping of Mammalian Follicle Development Using Brillouin Microscopy," *Communications Biology* 4, no. 1 (2021): 1133, https://doi.org/10.1038/s42003-021-02662-5.

101. C. Bevilacqua, H. Sánchez-Iranzo, D. Richter, A. Diz-Muñoz, and R. Prevedel, "Imaging Mechanical Properties of Sub-Micron ECM in Live Zebrafish Using Brillouin Microscopy," *Biomedical Optics Express* 10, no. 3 (2019): 1420, https://doi.org/10.1364/BOE.10.001420.

102. P.-J. Wu, M. I. Masouleh, D. Dini, et al., "Detection of Proteoglycan Loss From Articular Cartilage Using Brillouin Microscopy, With Applications to Osteoarthritis," *Biomedical Optics Express* 10, no. 5 (2019): 2457, https://doi.org/10.1364/BOE.10.002457.

103. Y. S. Ambekar, M. Singh, G. Scarcelli, et al., "Characterization of Retinal Biomechanical Properties Using Brillouin Microscopy," *Journal of Biomedical Optics* 25, no. 09 (2020): 1–7, https://doi.org/10.1117/1.JBO.25.9.090502.

104. A. Karampatzakis, C. Z. Song, L. P. Allsopp, et al., "Probing the Internal Micromechanical Properties of Pseudomonas aeruginosa Biofilms by Brillouin Imaging," *npj Biofilms and Microbiomes* 3, no. 1 (2017): 20, https://doi.org/10.1038/s41522-017-0028-z.

105. G. Lepert, R. M. Gouveia, C. J. Connon, and C. Paterson, "Assessing Corneal Biomechanics With Brillouin Spectro-Microscopy," *Faraday Discussions* 187 (2016): 415–428, https://doi.org/10.1039/C5FD00152H.

106. S. Ryu, N. Martino, S. J. J. Kwok, L. Bernstein, and S.-H. Yun, "Label-Free Histological Imaging of Tissues Using Brillouin Light Scattering Contrast," *Biomedical Optics Express* 12, no. 3 (2021): 1437, https://doi.org/10.1364/BOE.414474.

107. B. A. Loveless, K. A. Moin, P. C. Hoopes, and M. Moshirfar, "The Utilization of Brillouin Microscopy in Corneal Diagnostics: A Systematic Review," *Cureus* (2024), https://doi.org/10.7759/cureus.65769.

108. N. Shu, Y. He, and Y. Zhang, "Research Progress on Measurement Methods and Clinical Applications of Corneal Elastic Modulus," *Experimental Eye Research* 245 (2024): 109974, https://doi.org/10.1016/j.exer.2024.109974.

109. M. Al Bdour, H. M. Sabbagh, and H. M. Jammal, "Multi-Modal Imaging for the Detection of Early Keratoconus: A Narrative Review," *Eye and Vision* 11, no. 1 (2024): 18, https://doi.org/10.1186/s40662-024-00386-1.

110. Y. Ma, J. Cao, Y. Yu, et al., "Brillouin Assessment of the Crystalline Lens in Patients With High Myopia After Long-Term Implantable Collamer Lens V4c Implantation," *Acta Ophthalmologica* 103, no. 8 (2025): 1032–1040, https://doi.org/10.1111/aos.17435.

111. J. Xu, M. Liu, X. Lan, et al., "Brillouin Microscopic Imaging of Ex-Vivo Porcine Eye Using VIPA-CMOS-Based Spectrometer," *Measurement* 231 (2024): 114593, https://doi.org/10.1016/j.measurement.2024.114593.

112. H. Zhang, L. Asroui, J. B. Randleman, and G. Scarcelli, "Motion-Tracking Brillouin Microscopy for In-Vivo Corneal Biomechanics Mapping," *Biomedical Optics Express* 13, no. 12 (2022): 6196, https://doi.org/10.1364/BOE.472053.

113. H. Zhang, L. Asroui, I. Tarib, W. J. Dupps, G. Scarcelli, and J. B. Randleman, "Motion-Tracking Brillouin Microscopy Evaluation of Normal, Keratoconic, and Post–Laser Vision Correction Corneas,"

26999293, 2026, 11, Downloaded from https://advanced.onlinelibrary.wiley.com/doi/10.1002/adpr.202500132 by Emiliano Descrovi - ETH Zürich , Wiley Online Library on [06/11/2026]. See the Terms and Conditions (https://onlinelibrary.wiley.com/terms-and-conditions) on Wiley Online Library for rules of use; OA articles are governed by the applicable Creative Commons License

American Journal of Ophthalmology 254 (2023): 128–140, https://doi.org/10.1016/j.ajo.2023.03.018.

114. E. O. Wisniewski, P. Mistriotis, K. Bera, et al., "Dorsoventral Polarity Directs Cell Responses to Migration Track Geometries," *Science Advances* 6, no. 31 (2020): eaba6505, https://doi.org/10.1126/sciadv.aba6505.

115. X. Cao, E. Moeendarbary, P. Isermann, et al., "A Chemomechanical Model for Nuclear Morphology and Stresses During Cell Transendothelial Migration," *Biophysical Journal* 111, no. 7 (2016): 1541–1552, https://doi.org/10.1016/j.bpj.2016.08.011.

116. J. Zhang, X. A. Nou, H. Kim, and G. Scarcelli, "Brillouin Flow Cytometry for Label-Free Mechanical Phenotyping of the Nucleus," *Lab on a Chip* 17, no. 4 (2017): 663–670, https://doi.org/10.1039/C6LC01443G.

117. H. T. Nia, L. L. Munn, and R. K. Jain, "Physical Traits of Cancer," *Science* 370, no. 6516 (2020): eaaz0868, https://doi.org/10.1126/science.aaz0868.

118. M. Plodinec, M. Loparic, C. A. Monnier, et al., "The Nanomechanical Signature of Breast Cancer," *Nature Nanotechnology* 7, no. 11 (2012): 757–765, https://doi.org/10.1038/nnano.2012.167.

119. K. Hilai, D. Grubich, M. Akrawi, et al., "Mechanical Evolution of Metastatic Cancer Cells in 3D Microenvironment," *Small* 21, no. 18 (2025): 2403242, https://doi.org/10.1002/smll.202403242.

120. C. D. Paul, P. Mistriotis, and K. Konstantopoulos, "Cancer Cell Motility: Lessons From Migration in Confined Spaces," *Nature Reviews Cancer* 17, no. 2 (2017): 131–140, https://doi.org/10.1038/nrc.2016.123.

121. L. Martinez-Vidal, C. Testi, E. Pontecorvo, et al., "Progressive Alteration of Murine Bladder Elasticity in Actinic Cystitis Detected by Brillouin Microscopy," *Scientific Reports* 14, no. 1 (2024): 484, https://doi.org/10.1038/s41598-023-51006-2.

122. N. John, T. Fleming, J. Kolb, et al., "Biphasic Inflammation Control by Dedifferentiated Fibroblasts Enables Axon Regeneration After Spinal Cord Injury in Zebrafish," (2025), https://doi.org/10.1101/2025.01.27.635043.

123. W. Y. So, B. Johnson, P. B. Gordon, et al., "Macrophages Mediate Mesoscale Brain Mechanical Homeostasis," *Advanced Materials* 38, no. 6 (2026): e17493, https://doi.org/10.1002/adma.202517493.

124. M. Yao, R. Fuentes-Domínguez, S. L. Cavera, F. Pérez-Cota, R. J. Smith, and M. Clark, "Optoacoustic Lenses for Lateral Sub-Optical Resolution Elasticity Imaging," *Photoacoustics* 41 (2025): 100663, https://doi.org/10.1016/j.pacs.2024.100663.

125. J. Zhang, R. Raghunathan, J. Rippy, et al., "Tissue Biomechanics During Cranial Neural Tube Closure Measured by Brillouin Microscopy and Optical Coherence Tomography," *Birth Defects Research* 111, no. 14 (2019): 991–998, https://doi.org/10.1002/bdr2.1389.

126. Y. Su, H. Wu, L. Qiu, and W. Zhao, "Annular Pupil Confocal Brillouin–Raman Microscopy for High Spectral Resolution Multi-Information Mapping," *Nanophotonics* 12, no. 18 (2023): 3535–3544, https://doi.org/10.1515/nanoph-2023-0139.

127. Y. S. Ambekar, C. D. Caiaffa, B. J. Wlodarczyk, et al., "Optical Coherence Tomography-Guided Brillouin Microscopy Highlights Regional Tissue Stiffness Differences During Anterior Neural Tube Closure in the *Mthfd1l* Murine Mutant," *Development* 151, no. 10 (2024): dev202475, https://doi.org/10.1242/dev.202475.

128. Y. S. Ambekar, M. Singh, A. W. Schill, et al., "Multimodal Imaging System Combining Optical Coherence Tomography and Brillouin Microscopy for Neural Tube Imaging," *Optics Letters* 47, no. 6 (2022): 1347, https://doi.org/10.1364/OL.453996.

129. R. Mercatelli, S. Mattana, L. Capozzoli, et al., "Morpho-Mechanics of Human Collagen Superstructures Revealed by All-Optical Correlative Micro-Spectroscopies," *Communications Biology* 2, no. 1 (2019): 117, https://doi.org/10.1038/s42003-019-0357-y.

130. L. Qiu, Y. Su, K.-M. Xu, et al., "A High-Precision Multi-Dimensional Microspectroscopic Technique for Morphological and Properties Analysis of Cancer Cell," *Light: Science & Applications* 12, no. 1 (2023): 129, https://doi.org/10.1038/s41377-023-01153-y.

131. S. Kerdegari, A. A. Passeri, F. Morena, et al., "Artefact-Free Characterization of Nuclear Mechanics Using Correlative Brillouin-Raman Micro-Spectroscopy in Living Cells," 2024, https://doi.org/10.2139/ssrn.5050966.

132. A. B. Roberts, J. Zhang, V. Raj Singh, et al., "Tumor Cell Nuclei Soften During Transendothelial Migration," *Journal of Biomechanics* 121 (2021): 110400, https://doi.org/10.1016/j.jbiomech.2021.110400.

133. C. Shi, Y. Yan, M. Mehrmohammadi, and J. Zhang, "Versatile Multimodal Modality Based on Brillouin Light Scattering and the Photoacoustic Effect," *Optics Letters* 48, no. 13 (2023): 3427, https://doi.org/10.1364/OL.495361.

134. M. Nikolić, G. Scarcelli, and K. Tanner, "Multimodal Microscale Mechanical Mapping of Cancer Cells in Complex Microenvironments," *Biophysical Journal* 121, no. 19 (2022): 3586–3599, https://doi.org/10.1016/j.bpj.2022.09.002.

135. C. Handler, C. Testi, and G. Scarcelli, "Advantages of Integrating Brillouin Microscopy in Multimodal Mechanical Mapping of Cells and Tissues," *Current Opinion in Cell Biology* 88 (2024): 102341, https://doi.org/10.1016/j.ceb.2024.102341.

136. I. Remer, L. Cohen, and A. Bilenca, "High-Speed Continuous-Wave Stimulated Brillouin Scattering Spectrometer for Material Analysis," *Journal of Visualized Experiments* 127 (2017): 55527, https://doi.org/10.3791/55527.

137. Y. Qi, S. Yao, Z.-X. Du, et al., "Stimulated Brillouin Scattering Microscopy With a High-Peak-Power 780-Nm Pulsed Laser System," *Nature Photonics* 19, no. 8 (2025): 879–887, https://doi.org/10.1038/s41566-025-01697-y.

138. M. Mattarelli, M. Vassalli, and S. Caponi, "Relevant Length Scales in Brillouin Imaging of Biomaterials: The Interplay Between Phonons Propagation and Light Focalization," *ACS Photonics* 7, no. 9 (2020): 2319–2328, https://doi.org/10.1021/acsphotonics.0c00801.

139. L. Thévenaz, S. F. Mafang, and J. Lin, "Effect of Pulse Depletion in a Brillouin Optical Time-Domain Analysis System," *Optics Express* 21, no. 12 (2013): 14017, https://doi.org/10.1364/OE.21.014017.

140. J. Icha, M. Weber, J. C. Waters, and C. Norden, "Phototoxicity in Live Fluorescence Microscopy, and How to Avoid It," *BioEssays* 39, no. 8 (2017): 1700003, https://doi.org/10.1002/bies.201700003.

141. J. A. Willis, V. Cheburkanov, and V. V. Yakovlev, "High-Dose Photodynamic Therapy Increases Tau Protein Signals in Drosophila," *IEEE Journal of Selected Topics in Quantum Electronics* 29, no. 4: Biophotonics (2023): 1–8, https://doi.org/10.1109/JSTQE.2023.3270403

142. Y. Xiang, C. Basirun, J. Chou, et al., "Background-Free Fibre Optic Brillouin Probe for Remote Mapping of Micromechanics," *Biomedical Optics Express* 11, no. 11 (2020): 6687, https://doi.org/10.1364/BOE.404535.

143. G. Antonacci, K. Elsayad, and D. Polli, "On-Chip Notch Filter on a Silicon Nitride Ring Resonator for Brillouin Spectroscopy," *ACS Photonics* 9, no. 3 (2022): 772–777, https://doi.org/10.1021/acsphotonics.2c00005.

144. P. Bradbury, A. Cidem, H. Mahmodi, et al., "Timothy Grass Pollen Induces Spatial Reorganisation of F-Actin and Loss of Junctional Integrity in Respiratory Cells," *Inflammation* 45, no. 3 (2022): 1209–1223, https://doi.org/10.1007/s10753-021-01614-9.

26999293, 2026, 11, Downloaded from https://advanced.onlinelibrary.wiley.com/doi/10.1002/adpr.202500132 by Emiliano Descrovi - ETH Zürich , Wiley Online Library on [06/11/2026]. See the Terms and Conditions (https://onlinelibrary.wiley.com/terms-and-conditions) on Wiley Online Library for rules of use; OA articles are governed by the applicable Creative Commons License